University of Cologne

Faculty of Mathematics and Natural Sciences

Institute for Geophysics and Meteorology

Master thesis

Snowfall rate retrieval from ground-based in situ and radar measurements

Sybille Yvonne Schoger

1. Supervisor:

Prof. Dr. Susanne Crewell

2. Supervisor:

Dr. Kerstin Ebell

submitted

27.05.2019

edited 28.08.2019

Abstract

Snow makes up a large portion of the hydrological cycle. Its impact on the climate, especially in the Arctic is of particular interest due to the observed Arctic Amplification - the enhanced warming in the Arctic compared to the global mean. Measurements of solid precipitation are prone to large uncertainties due to the complex microphysical structure of snow particles. In situ measuring precipitation gauges underestimate the snow accumulation at windy conditions. Radar-based snowfall rate estimates have been traditionally derived from an equivalent reflectivity (Z_e) - snowfall rate (S) power law relationship. It is known to have a wide parameter variation due to changes in snow properties such as mass and particle size distribution (PSD) for each individual snowfall event. Thus, an accurate observation of the snowfall rate is still challenging.

In this work, radar simulations and observations at two frequencies are utilized: K-Band (24 GHz) and W-Band (94 GHz) combined with surface disdrometer measurements. The aim is twofold: First, the derivation of the prefactor and exponent for a Z_e-S relationship from simulated Z_e: a snowfall rate retrieval development. Second, the application of these parameters to measured Z_e.

The retrieval development is performed using ground-based in situ measurements of a video-disdrometer operating at the meteorological station in Hyytiälä, Finland. Snow event measurements during two winters in 2014/2015 include PSD, velocity and derived masses of snowflakes to calculate the snowfall rate. To obtain Z_e two forward models were used for the calculation of the backscatter cross section. The models were performed using T-Matrix Method to describe soft spheroids for K-Band and using a single scattering database from Discrete Dipole Approximation of realistic snowflakes for W-Band. To examine different dependencies of the Z_e-S relationship parameters, the PSD was approximated with an exponential function, using N_0 as the intercept parameter. An uncertainty analysis reveals that for K-Band the snowfall rate estimation is significantly improved by including N_0: the RMSE of around 0.34 mm/h for an average Z_e-S relationship is reduced to a mean of approximately 0.15 mm/h. For W-Band a relationship with averaged parameters over a longer time period shows the best result with a RMSE of 0.15 mm/h.

The retrieval parameters are applied to measured Z_e of the Micro Rain Radar (MRR, K-Band) and the Microwave Radar for Arctic Clouds (MiRAC, W-Band) at the research base in Ny Ålesund, Svalbard. Additionally, for the calculation of N_0, measurements of a laser-disdrometer at this site are used.

Five days from January to March 2018 are evaluated in detail. In general, the snowfall rate calculations from MRR and MiRAC agree well. However, a comparison of the calculated snow accumulation values from the radars to gauge measurements deviate from one another.

Contents

1 Introduction

Solid precipitation and its deposition as snow are of great importance for the Earth's energy budget and its hydrological cycle. The albedo of a snow covered surface is highest compared to other natural surfaces. Due to low thermal conductivity and high reflectivity, snowfall and the resulting snow cover can prevent the melting of underlaying ice in summer, but it can also inhibit sea ice growth in winter (*Merkouriadi* et al., 2017). Further the ice mass balance is affected by snowfall regime changes and in general interlinked with many complex ecological and hydrological processes, human activities, infrastructure, biodiversity and most important for atmospheric sciences, with a changing climate (*AMAP*, 2011). Global warming is two times faster in the Arctic than anywhere else on Earth (*IPCC*, 2007; *Serreze and Barry*, 2011), known as Arctic Amplification. Thus, the observation of snowfall in the Arctic is of particular interest.

In the Svalbard archipelago long-term measurements are available, from which *Førland* et al. (2012) evaluated temperature and manual precipitation gauge observations as well as projections for the years 1900-2100. The authors found a total annual average precipitation amount of 427 mm between the years 1981-2010 in Ny-Ålesund on Spitsbergen, one of Svalbard's islands. This amount is already 20% higher than in the period 1961-1990 and they predict an even higher increase until the next century.

The latest reanalysis product ERA5 (*Hersbach and Dick*, 2016) from the European Centre for Medium-range Weather Forecast (ECMWF), currently has the highest temporal and spatial resolution of any former reanalyses, and might be a more reasonable measure for a continuous representation of manifold variables in remote regions than e. g. point measurements from gauges. Within a reanalysis, available observations are combined with numerical models and with this data assimilation information about the recent climate are provided.

The accumulation of total precipitation and snowfall of ERA5 data at Ny-Ålesund for the year 2018 shows the importance of snowfall in the Arctic (Figure 1.1). Almost three-quarters of the accumulated total precipitation (912.06 mm) is snow (674.41 mm). Rain is calculated from their difference. A larger spread for snowfall in comparison to the total precipitation, between the closest grid point (79°N, 12°E) to Ny-Ålesund and eight surrounding grid points, is most likely due to the different orography at which the grid points are located. Ny-Ålesund is located at the west coast of Svalbard, close to the open sea and right next to a Fjord. Also, the island Spitsbergen is in general very mountainous.

While in the ERA5 data solid precipitation clearly dominates the total precipitation,
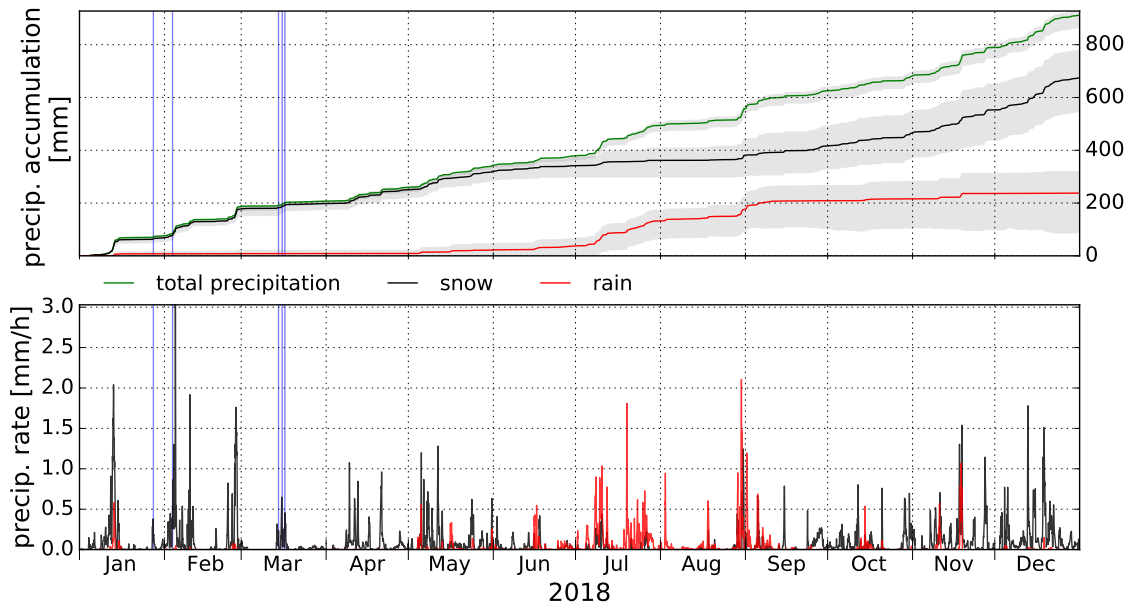
Figure 1.1: For 2018 the total precipitation (green) and the snowfall (black) data from the ECMWF reanalysis ERA5 are accumulated for the closest grid point (79°N, 12°E) to Ny-Ålesund. The grey shading displays the spread of the accumulated values from eight surrounding grid points. The difference between total precipitation and snowfall is the total rain amount (red) as well as the grey shaded spread. The vertical blue lines indicate five days analysed in more detail in Section 6.

warmer temperatures indicated more rain rather than snowfall events in the Arctic which has been detected over the last decades (*López-Moreno* et al., 2016; *Maturilli* et al., 2013).

The observation and modeling of precipitation, notably snow, is still a big challenge and affected by different uncertainties. Especially in the Arctic an observational network is scarce and the environmental conditions such as weather and orography are harsh for instrumentation. In this region, reanalyses have to rely more heavily on models, which also suffer from uncertainties due to still incomplete microphysical knowledge of clouds and precipitation and their simplified and parameterized mathematical implementation. Additionally, different reanalyses are inconsistent in their spatial representation of precipitation trends (*Lindsay* et al., 2014).

To obtain in situ real-time information on a global scale and to validate models, gauges are the main instruments to measure precipitation at the surface. One particular problem with gauges, especially for solid precipitation, is that they either have an undercatch of snow due to high winds or an overcatch due to blowing snow. Wind shields are a method to enhance the catch efficiency of gauges by reducing the airflow around them (*Rasmussen* et al., 2012). Within the "Solid Precipitation Intercomparison Experiment" (SPICE)[1], organized by the World Meteorological Organization (WMO) Commission for Instruments and Methods of Observation

---

[1] http://www.wmo.int/pages/prog/www/IMOP/intercomparisons/SPICE/SPICE.html

(CIMO), which took place between 2012-2015, *Nitu* et al. (2018) investigated automatic gauges to improve their measurement reliability and to better understand solid precipitation. Despite the necessity for continuous climatological, but also real-time surface measurements, gauges are limited in their spatial resolution as they only provide information from a specific (point) position at the surface.

Radio detecting and ranging (radar) observations use electromagnetic radiation to scan the atmosphere either vertically or with an azimuth angle. Thus, they have the ability to look at an increasing atmospheric volume and to measure over greater distances. The derived property from the transmitted, backscattered and then received power signal at the radar is the equivalent radar reflectivity Z_e (often just referred to as: reflectivity). However, the precipitation rate, which can be directly measured by a gauge, is needed. To connect radar observations with surface measurements, radar-based snowfall estimates are traditionally retrieved via the power law $Z_e = a_{zs} S^{b_{zs}}$, with the snowfall rate (S), prefactor a_{zs} and exponent b_{zs}. As the pioneers *Langille and Thain* (1951) calculated the reflectivity from measured snowfall rate values to connect them to measured reflectivity values, the equation has been historically kept this way. Nowadays, one is more interested in the opposite, the snowfall rate calculated from the reflectivity with empirically derived parameters. More than 60 years of research has authored many publications on different Z_e-S relationship parameters (e.g. *Langille and Thain*, 1951; *Marshall and Gunn*, 1952; *Imai* et al., 1955; *Fujiyoshi* et al., 1990; *Rasmussen* et al., 2003; *Huang* et al., 2010; *Heymsfield* et al., 2016; *von Lerber* et al., 2017). Surface observations have been evaluated with different radars using different wavelengths λ. Due to the complex structure of snow particles, their microphysical properties are strongly variable. Thus, for each snow event, each measurement location and each radar wavelength used, the parameters of the Z_e-S relationship differ significantly.

In the first few decades weather radars, operating at centimeter-wavelengths ($\lambda = 3 - 10$ cm), were typically used for quantitative precipitation estimates (QPE). In general, rain particles can be approximated as spheres (with diameter D). Within Rayleigh scattering ($D \ll \lambda$) the radar reflectivity of a sphere is approximately the sixth power of D. However, snowflakes are non-spherical and thus the more generalized *equivalent* radar reflectivity is calculated from the backscatter cross section of the particle. For weather radar measurements manifold Z_e-S relationships with the prefactor a_{zs} ranging between values of 160 to 3300 and b_{zs} between 1.5 and 2.2 are available and are summarized by *Rasmussen* et al. (2003). Within a theoretical analysis they furthermore showed dependencies of the parameters a_{zs} and b_{zs} on microphysical snow properties (e.g. crystal type).

Lhermitte (1987; 1988) was one of the first to propose a millimeter-wavelength radar (λ = 3.19 mm, f = 94 GHz, W-Band) to study clouds and precipitation. Using electromagnetic radiation with this wavelength, large observed hydrometeors are likely to be of the same size D as the wavelength. Thus, the scattering properties of the observed cloud particles, liquid or solid precipitation change from Rayleigh to Mie scattering (D $\sim \lambda$). *Kollias* et al. (2002) thoroughly investigated the question why Mie scattering is of great importance for the application of millimeter-wavelength radar measurements for QPE. A broader overview of the research activities with millimeter-wavelength radars can be found in *Kollias* et al. (2007) and references therein.

In 2006 the satellite CloudSat (*Stephens* et al., 2002) was launched, with its W-Band Cloud Profiling Radar (CPR). For the first time it became possible to retrieve a global estimate of snowfall (*Kulie and Bennartz*, 2009; *Liu*, 2008), especially over the polar regions. But, radar measurements from space lack accuracy of surface information. A so called "blind zone", from 1200 m down to the surface, inhibits reliable reflectivity observations due to ground clutter. Snowfall statistics were evaluated for Ny-Ålesund and Princess Elisabeth station, Antarctic, as part of a comparison study of CPR and a Micro Rain Radar (MRR, λ = 12.38 mm, f = 24 GHz, K-Band) at the surface by *Maahn* et al. (2014). Within the blind zone they found an underestimation of the radar reflectivity by about 1 dB and ca. 10% underestimation of precipitation amount.

From June 2016 to October 2018 the University of Cologne (UoC) has provided a W-Band cloud radar to the French-German Arctic research station AWIPEV (Alfred Wegener Institut for Polar and Marine Research (AWI) and Institute Paul Emile Victor (IPEV)) at Ny-Ålesund. Additionally, since April 2017 continuous observations are available from a MRR and a laser-disdrometer. The instruments were installed within the framework of the Transregional Collaborative Research Center (TR 172) project[2]: "Arctic Amplification: Climate Relevant Atmospheric and Surface Processes, and Feedback Mechanisms (AC)[3]" in which the UoC collaborates with multiple partners.

With the newly installed radars, similar to the comparison of MRR with CPR by *Maahn* et al. (2014), it is possible to compare MRR measurements just now with a surface-based W-Band radar. For Ny-Ålesund no Z_e-S relationship could yet be derived due to inadequate instrumentation for snow observations and the lack of a longer continuous time series. Although two radars are now available at Ny-Ålesund, surface-based instruments that capture the complex snow microphysics accurately

---

[2] `http://www.ac3-tr.de`

are missing. Furthermore for a radar with the frequency of 24 GHz, a Z_e-S relationship has been mostly calculated from a relationship for a 35 GHz radar in the past (e. g. *Kneifel* et al., 2011b; *Maahn* et al., 2014). Thus, the thesis has two main objectives:

First, the derivation of the prefactor and exponent of the Z_e-S relationship for simulated K-Band (24 GHz) and W-Band (94 GHz) radar reflectivities: the development of a snowfall rate retrieval.

Second, the application of these derived parameters to measured K- and W-Band radar reflectivities as well as the evaluation of the resulting snowfall rate among the two radars and with in situ observations.

For the first part, a cooperation with the University of Helsinki, namely with the Associate Professor Dmitri Moisseev, offered the possibility to derive a new Z_e-S relationship for a 24 GHz and a 94 GHz radar with a dataset from the meteorological station in Hyytiälä, Finland, the closest station to Ny-Ålesund feasible. At Hyytiälä, more accurate snow properties could be obtained from a video-disdrometer than from the available laser-disdrometer in Ny-Ålesund. In the second part, the derived parameters are applied to the Z_e measurements from MRR and the Microwave Radar for Arctic Clouds (MiRAC). For the evaluation of the results two questions emerge: How well do the calculated snowfall rates agree with one another? How well is the agreement with gauge measurements, when comparing the snowfall accumulation?

The structure of this thesis is as follows: In Section 2, a broad insight in the microphysics of snow is given. Section 3 introduces the two measurement sites from which instrument data are used. Different in situ, surface and radar instrumentation are described in detail in Section 4. The methodology of the snowfall rate retrieval development at the site in Hyytiälä - how two different Z_e-S relationships have been derived - is explained in Section 5. The application of the Z_e-S relationship parameters to the two radars at Ny-Ålesund from which the resulting snowfall rates are evaluated with other observations are discussed in Section 6. Finally, Section 7 completes the thesis with a summary and an outlook.

2 Snow microphysics

Snow particles can have many forms, thus different densities and can range between sizes of 0.1 millimeters to a few centimeters. The variety originates from different growth processes. Single particles may be coarsely divided into plates and columns. Their subdivision is much more diverse, as the general process of snow crystal growth can be divided into water vapor deposition, aggregation or riming. Aggregation leads to the form of snowflakes and results from two snow crystals colliding with each other. Rimed particles form when snow crystals collide with supercooled liquid drops which directly freeze by contact, which could lead to formation of graupel. (*Pruppacher and Klett*, 1997) For the growth process the environmental
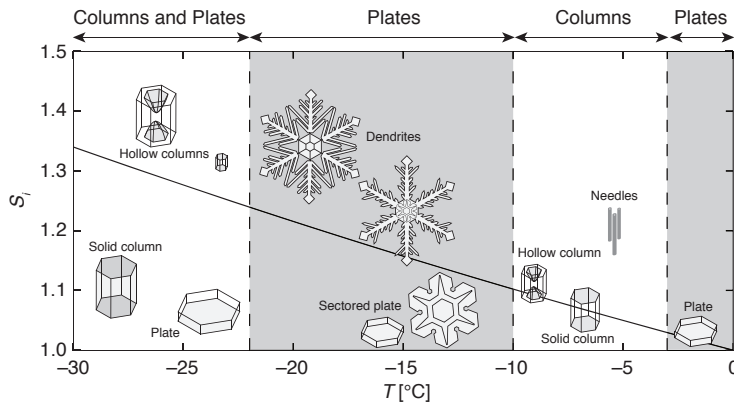
Figure 2.1: Ice crystal morphology or Nakaya diagram: The division of different ice crystal habits dependent on their formation in the atmosphere as a function of temperature and supersaturation. The black line shows the saturation line with respect to water. (*Lohmann* et al. (2016), Fig 8.15)

atmospheric conditions such as temperature and humidity are important. When the relative humidity exceeds 100%, the atmosphere is considered to be supersaturated. Temperature and supersaturation change the crystal structure. An experiment in a laboratory, where synthetically grown single snow crystals have been observed and categorized under different temperatures and supersaturation values, was carried out by the Japanese physicist Ukichiro Nakaya in the 1930s (summarized in *Libbrecht* (2005)). Named after him, the Nakaya diagram (Figure 2.1) presents different types of snow crystals which grow in distinct temperature and supersaturation ranges. It is also referred to as the snow crystal morphology diagram, which further shows that for higher supersaturation the complexity of the crystal structure increases. Plates form at temperatures from 0°C to 3°C and again between -10°C and -22°C. Columns form between -3°C and -10°C and are also predominantly present at temperatures below -22°C although at these low temperatures a combination of both, plates and columns, can be found.

If an ensemble of ice crystal particles, e.g. the aggregated or (heavily) rimed snowflake (left side of Figure 2.2, top and bottom, respectively) is regarded, it can be seen that they differ in their dimension and structure, which affects their den-

Figure 2.2: Aggregated (top) and heavily rimed (bottom) snowflake images at a single-view from the Multi-Angle Snowflake Camera (MASC) (left) with their white perimeter projection (right). The red circle describes the area equivalent to the white snowflake area. In magenta (solid) the maximum diameter (along major axis) of the snowflake and the orientation angle (dotted) of the major axis with respect to the horizontal is shown. (*Gergely* et al., 2017)
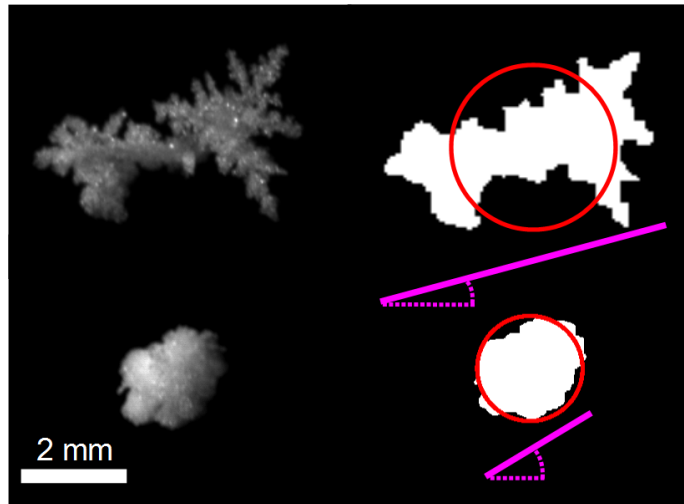

sity and thus, their mass and fall velocity (*Gergely* et al., 2017). These properties are some of the microphysical parameters, that are of importance when it comes to describe snowfall and will be discussed in the following sections. Investigating these microphysical properties will help to understand and explain the interactions between hydrometeors and atmospheric dynamics as well as thermodynamics better (*Pruppacher and Klett*, 1997). A more detailed characterization of the microphysical properties and processes of snow crystals can be read in-depth e. g. in *Pruppacher and Klett* (1997); *Lohmann* et al. (2016).

In the following sections a brief wrap-up shall set the basis of the important physical description of snow particle diameter (Section 2.1), the closely linked mass and fall speed (Section 2.2) as well as the particle size distribution (Section 2.3). The knowledge of these properties is needed for the radar-based snowfall rate retrieval (Section 2.4). For the latter, scattering, as a major radiation process when working with radar, is briefly discussed and two different scattering regimes and methods are introduced (Section 2.5.1 and 2.5.2, respectively).

2.1   Particle dimension

Due to the complex structure of snowflakes and the used measurement technology, the dimension of the particle can have different definitions. Picture-taking instrumentation extract the perimeter of the snowflake (example in Figure 2.2). From this, either the maximum diameter or the area-equivalent circle can be derived. The maximum diameter can be explained as the circumscribed sphere diameter (D_{max} in Figure 2.3, left) or as the diameter of the major axis when assuming the snowflake to be approximately an ellipse in 2D (D_{maj} in Figure 2.3, right). The area of the circular disk, that is described with the area- or sometimes also disk-equivalent-

diameter, is of the same size as the area of the mapped snowflake image (D_{deq} in Figure 2.3, left). The snowfall rate retrieval in this work (Section 5) was done by using the disk-equivalent diameter of the measured particle.
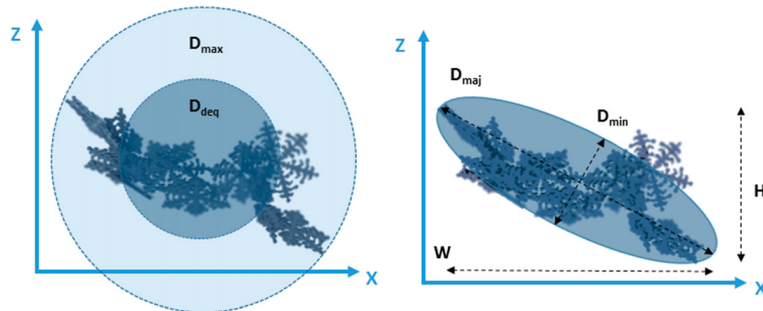
Figure 2.3: Schematic plane projections of an aggregated snowflake in side view with the disk-equivalent (D_{deq}), the maximum (D_{max}) diameter (top), the major and minor diameter of a fitted ellipse as well as the maximum height H and width W of the particle. (*von Lerber* et al., 2017)

2.2   Particle mass and fall velocity

Describing snow crystals by their bulk density involves many uncertainties due to the irregular shape of the particle. Mass is more straightforward to observe and thus empirical mass-size relationships have been derived (e.g. *Pruppacher and Klett*, 1997). Although the approximation of an empirical relationship is prone to uncertainties as well, nowadays it is important for numerical weather and climate models to use a mass-size relationship to characterize snow. Furthermore, radar signatures are linked to aggregated or rimed particles, which are dependent on their change in mass (e.g. *Gergely* et al., 2017; *Leinonen and Moisseev*, 2015). Thus, mass is one of the main microphysical properties. The mass-size relation is generally approximated in the power law format

$$m(D) = a_m D^{b_m}. \tag{1}$$

With mass in grams and dependent on the unit of the used diameter, here assumed millimeters, the prefactor then is in g mm$^{-b_m}$, whereas the exponent is unitless and usually in the range of $0 < b_m \leq 3$. Most of the snow particles, which have a low-density, have a mass exponent of about 2. Towards the upper end of this exponent range the density increases and thus describes particles such as graupel.

The derivation of the coefficients a_m and b_m was historically done empirically (e.g. *Magono and Nakamura*, 1965; *Pruppacher and Klett*, 1997; *Locatelli and Hobbs*, 1974), or mathematically with the theory of hydrodynamics (*Böhm*, 1989). The latter method was originally developed to derive the terminal fall velocity from mass and the area projected to the airflow of the falling hydrometeor. From the inverse calculation mass can be retrieved. The relationship of the so-called Best

number (*Pruppacher and Klett*, 1997) and the Reynolds number is needed. With a least square fit in log-space, the two power-law parameters for mass are determined empirically.

Another important microphysical property is the fall velocity, which is dependent on mass, aerodynamic drag, the shape of the snow particle and its orientation. Regarding the manifold snowflake shapes, the fall velocity can range from 0.5 m/s to 2 m/s. Similar to the mass, the fall velocity can be determined empirically by measuring or mathematically with the hydrodynamic theory (*Böhm*, 1989). Using a dataset of measured fall velocities, e. g. from a disdrometer, a fairly well approximation can also be formulated as power-law:

$$v(D) = a_v D^{b_v}. \tag{2}$$

For the prefactor a_v [m/s mm$^{-b_v}$] *Locatelli and Hobbs* (1974) found values in the range of 0.62 to 1.5 and the dimensionless exponent b_v differs from 0.12 to 0.66. *Szyrmer and Zawadzki* (2010) and *Tiira* et al. (2016) have found an exponent of around 0.2 for low-density snowflakes, which is used as a fixed value in later calculations.

2.3 Particle size distribution

Within a given particle size interval, the particle number concentration is expressed as the particle size distribution (N(D) or PSD). Typically for snow N(D) [mm^{-1} m^{-3}] can be approximated with an exponential function (*Gunn and Marshall*, 1958)

$$N(D) = N_0 \, exp(-\Lambda D) \tag{3}$$

with the intercept parameter N_0 [mm^{-1} m^{-3}], the slope parameter Λ [mm^{-1}] and the particle diameter D [mm]. Whereas for rain the intercept parameter was found to be rather constant (*Marshall and Palmer*, 1948), it was not anymore for snow events, because it is a function of the precipitation rate (*Gunn and Marshall*, 1958).

Analytically the intercept parameter can be calculated with the method of moments (e. g. *Moisseev and Chandrasekar*, 2007) for which a measured PSD is necessary, then the nth moment can be calculated as:

$$M_n = \int_0^\infty D^n \, N(D) dD. \tag{4}$$

When inserting (3) in (4) and applying the complete Gamma function

$$\Gamma(n+1) = \int_0^\infty exp(-t)\, t^n\, dt \tag{5}$$

the analytical solution for the moment is obtained:

$$M_n = N_0\, \Lambda^{-(n+1)}\, \Gamma(n+1). \tag{6}$$

When relating different moments, the parameters of the particle size distribution can be calculated. E. g. *Moisseev and Chandrasekar* (2007) used the 2nd and 4th moment; in this work it is additionally assumed that the shape parameter μ is zero and thus the following formulas can be used to calculate the slope parameter Λ:

$$\Lambda = \sqrt{\frac{M_2 * \Gamma(5)}{M_4 * \Gamma(3)}} \tag{7}$$

and intercept parameter N_0:

$$N_0 = \frac{M_2 * \Lambda^3}{\Gamma(3)} \tag{8}$$

2.4   Radar-based snowfall rate retrieval

The snowfall rate in the water equivalent units of mm/h can not only be measured but also calculated from the previously mentioned microphysical properties:

$$S = \frac{3600}{\rho_w} \int_{D_{min}}^{D_{max}} m(D)v(D)N(D)dD \tag{9}$$

with the density of liquid water ρ_w, the mass-size relationship m(D) and the terminal velocity-size relationship v(D).

For radar meteorology the quantitative precipitation estimate (QPE) is important not only in weather and climate models, but also for hydrological services and nowcasting. To derive rain- or snowfall intensities, the latter has been done from an empirically determined power-law with a wide range of parameter values. Finding good values to derive a reliable QPE is an ongoing challenging research topic.

Reflectivity (Z_e), a quantity derived from the power measured by radar (Section 4.2) and the in situ measured snowfall rate (S) can be connected via the Z_e-S relationship, which is usually done by a simple regression fit through a scatterplot of snowstorm events:

$$Z_e = a_{zs}S^{b_{zs}}. \tag{10}$$

Due to the complex microphysics of snow, the correct estimation of snowfall from radar measurements remains especially challenging as the parameter values for the Z_e-S relationship are numerous and typically event-specific.

2.5 Scattering

When working with radar measurements important processes such as the scattering interactions between the electromagnetic wave of the radar and the observed hydrometeors (in this work: snow particles) have to be understood. In general, scattering is the re-emission of incident electromagnetic radiation on a particle. Particles are considered to consists of dipoles which get excited by the incoming electromagnetic wave. The dipole charges begin to oscillate and transmit a secondary electromagnetic wave into a specified direction, depending on the size of the particle and the incoming wavelength.
In the following a short overview of two important scattering regimes and how two models are estimating the scattering properties of single snow crystals are given.

2.5.1 Scattering regimes

The size of the hydrometeor and the utilized wavelength of the incident electromagnetic wave are related to each other by the dimensionless size parameter $\chi = \pi \, D / \lambda$. When plotting χ as a function of the particle dimension against wavelength, three different scattering regimes can be identified (Figure 2.4): Geometric optics ($\chi >$ 2000), Mie ($0.2 < \chi < 2000$), Rayleigh ($0.002 < \chi < 0.2$) (*Petty*, 2006).

Figure 2.4: Size parameter χ as a function of wavelength λ and particle radius. Dashed lines indicate the different scattering regimes. Examples of atmospheric particles are given on the right. A narrow grey vertical band displays the visible spectrum (VIS) with properties depending on the particle radius. Two wider grey vertical bands display the wavelength range at which cloud and precipitation radars operate. (*Lohmann* et al., 2016, Fig 9.5)
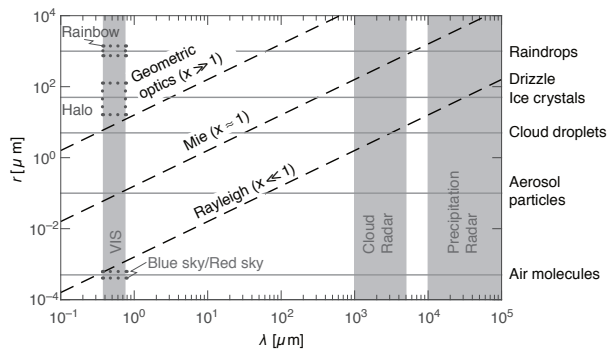
For a size parameter $\chi < 0.002$, scattering is negligible (below the lowest dashed line). For cloud and precipitation radars (grey bands to the right of Figure 2.4) two scattering regimes are important:

Rayleigh regime

When the particle size is much smaller than the wavelength (D $\ll \lambda$), which can be approximated as 1/16 of λ (*Lohmann* et al., 2016), scattering processes take place in the Rayleigh regime ($\chi \ll 1$). The scattering of radiation within this regime is equally distributed in the forward and backward direction and strongly proportional to the inverse of the fourth power of the wavelength (*Petty*, 2006). For instance in the visible spectrum radiation scattered on air molecules causes a blue sky during the day, which is owing to the strong wavelength dependency.

Mie or Resonance regime

In the Mie or also Resonance called scattering regime ($\chi \approx 1$), the scattered particle and the emitted wavelength are considered to be of the same size (D $\approx \lambda$). Forward scattering is the prevailing scattering direction. Summarized from *Kneifel* (2011), in Mie compared to Rayleigh regime, the phase of the propagating wave cannot be considered constant inside the scattering particle and therefore its dipoles experience phase differences at a specific time leading to interferences and complex scattering patterns altogether.

2.5.2   Scattering methods

Most of the frozen particles in the atmosphere are usually non-spherical. Thus, for further scattering calculations and investigating on QPE, assumptions and approximations about the scattered particles have to be made. In the following, two well-known methods will be introduced, summarizing from the doctoral thesis of *von Lerber* (2018).

T-Matrix Method (TMM)

The TMM calculates the T-Matrix in which particle property information and scattering characteristics are contained. It is used for homogeneous soft spheroids, which means the mixture of ice and air within a spheroid. Although the TMM is applicable not only for (non-)spherical particle shapes, the rotational symmetry is of great importance for an efficient and fast computation. Thus a significantly reduced calculation time and the simplicity of TMM is only then valid when using rotationally symmetric or spheroidal particles (*Mishchenko*, 2000). Another advantage is the independency of T-matrix elements in orientation of the electric fields, leading to only one calculation of the matrix which is then simply used for any radiation directions.

Discrete Dipole Approximation (DDA)

The DDA is a more complex and computationally time consuming scattering model but it can realistically derive the scattering characteristics of a snowflake. It is mostly used for computations in Mie regime and can be applied to particles that are inhomogeneous, anisotropic and shaped arbitrarily.

As one of the volume integral equation methods, the concept of the DDA is that the scatterer is partitioned into finite volume elements, which each represent a point dipole. The name DDA originates from the interpretation that a dipole moment is induced into these discrete volume elements by the effect of the excited electric field (*Kahnert*, 2003). Reducing the complexity of the particle with the approximation of homogeneous finite volumes, in which the electric field is assumed to be constant, and solving a resulting system of linear equations with standard techniques is a major advantage. However, increasing the number volume elements increases the equations and thus also computational time. Another drawback is that for each angle of incidence the scattering calculations have to be recalculated.

3   Measurement sites

Data was gathered from two different sites. For the derivation analysis of the Z_e-S relationship, data from the University of Helsinki, measured at the forestry field station Hyytiälä, Finland, were provided. Further analyses and evaluations were done with measurements at the station in Ny-Ålesund, Svalbard. An overview of both stations will be given in the following.

3.1   Hyytiälä

Figure 3.1: Meteorological measuring site in Hyytiälä, Finland, view from north.
Photo: Sybille Y. Schoger, September 2018

The University of Helsinki operates a Forestry Field Station in southern Finland, in Hyytiälä (61.8439°N, 24.2875°E, 150 m above mean sea level), 220 km North-West of Helsinki (*Hari and Kulmala*, 2005). Next to many instruments that measure aerosol properties within the forest (since 1962), recently installed meteorological instrumentation (since 2014) operate in the middle of a clearing, 20 metres away from trees (Figure 3.1) and close to a lake (to the right, outside of Figure 3.1).
Some of the in situ/surface instruments for precipitation measurements, installed in 2014, are the following: A precipitation gauge stands within a wind protection fence similar to the standard one of the WMO (the double fence intercomparison reference), and is in addition wind shielded with a single Alter shield. Also within the fence are a 2D video disdrometer (*Kruger and Krajewski*, 2002), perpendicular towards each other two laser-disdrometer PARSIVEL (PARticle SIze VELocity), and a 3D wind anemometer. Outside the fence is another 3D anemometer and gauge with a double Alter windshield. To measure snow, the video-disdrometer Particle Imaging Package (PIP, Section 4.1.1) for falling particles and an optical snow depth

sensor for snow amount at the ground, are in use.

As for the remote sensing instrumentation two radiometer and four radars are in operational use: C-Band (installed 2016), a W-Band and a transportable Ka-Band (both, since 2017) as well as a Micro Rain Radar (installed in 2014).

3.2   Ny-Ålesund
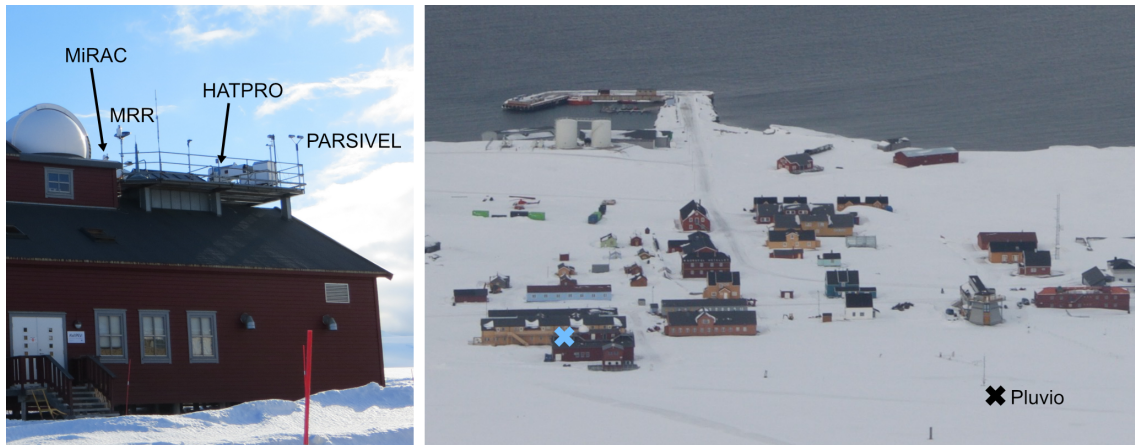
Figure 3.2: left: AWIPEV observatory, with remote-sensing instrumentation on the roof: Microwave Radar for Arctic Clouds (MiRAC, in the back), Micro Rain Radar (MRR), Humidity and Temperature Profiler (HATPRO) and laser-disdrometer PARticle SIze VELocity (PARSIVEL); right: View from Zeppelin-Mountain (south-west) onto the village Ny-Ålesund and part of the Kongsfjord; blue cross: AWIPEV observatory; red cross: location of precipitation gauge Pluvio. Photo left: Kerstin Ebell, April 2017; Photo right: Pavel Krobot, April 2017

Ny-Ålesund is a village with over a hundred years of research activity and plays an important role in monitoring the Arctic climate. Its location is in the Norwegian archipelago Svalbard on the island of Spitsbergen at a latitude of almost 79°N (78.9230°N) and a longitude of 11.9210°E. Ny-Ålesund is right next to the sea (Figure 3.2), situated at the Kongsfjord, at the west coast of Spitsbergen. The village is close to mountains which are located parallel to the Fjord from north-west, south to south-east. Ny-Ålesund is thus in a valley and just 11 m above sea level.

In 1991 the German research station from Alfred Wegener Institut (AWI, former Koldewey Station) was officially opened and is in operational use since then. The Rabot Station is operated since 2001 from the French Polar Institute Paul Emile Victor (IPEV). Both stations merged in 2003 and the now so called AWIPEV station does research activities in atmospheric physics, in marine and terrestrial biology and geosciences. A more detailed description of the historic development to the AWIPEV site can be found in *Neuber* (2006) from which the previous paragraph has been summarized.

Since 2016 the University of Cologne (UoC) collaborates with the University of Bremen and Leipzig as well as with AWI and the Leibniz Institute for Tropospheric Research in the Transregional Collaborative Research Centre (TR 172) project: "ArctiC Amplification: Climate Relevant Atmospheric and SurfaCe Processes, and Feedback Mechanisms (AC)[3]". Within this project the UoC operated a cloud radar (Section 4.2.1) from June 2016 to October 2018 in Ny-Ålesund and has ongoing measurements from a MRR (Section 4.2.2) and a laser-disdrometer PARSIVEL (Section 4.1.2) since April 2017. These instruments are located on the roof of the AWIPEV observatory (Figure 3.2 (left) and blue cross in Figure 3.2 (right)).

In August 2017, the precipitation gauge Pluvio (Section 4.1.3) was installed approximately 200 m away from the AWIPEV observatory roof in an open field (black cross in Figure 3.2 (right)).

Additionally, within the Baseline Surface Radiation Network (BSRN), the AWI has a longterm dataset on radiation since 1992 (*Maturilli* et al., 2013). Measurements from a 10 m tower (right above black cross in Figure 3.2) which include wind and temperature at 2 m and 10 m height are available from the BSRN site and used in this work to get an overview about the synoptical conditions during the evaluated case studies in Section 6. Detailed description about the meteorological sensors installed on the tower can be found in *Maturilli* et al. (2013).

4 Instrumentation

The snowfall rate retrieval development was done with observations and simulations from Hyytiälä and the resulting Z_e-S parameters were applied to radar measurements and compared to surface observations from Ny-Ålesund. An overview of the used instruments and details of their measuring principles is given in the following. A summary table (Table **??**) in the end of this section displays measured and derived variables from all instruments as well as the input/output of the used scattering models.
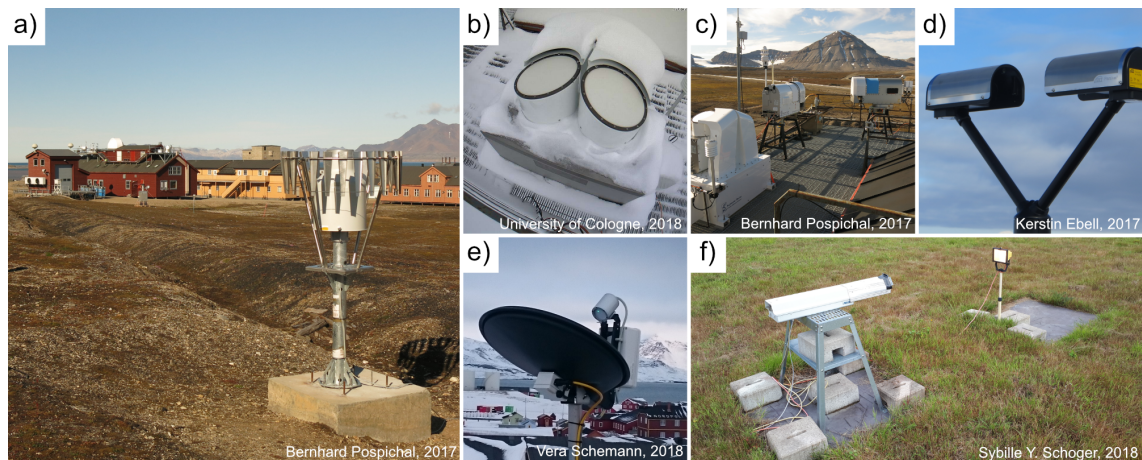
Figure 4.1: a) in the front: precipitation gauge Pluvio, in the background left: AWIPEV observatory; b) Microwave Radar for Arctic Clouds (MiRAC) from top; c) front left: MiRAC, middle: Microwave Radiometer for Arctic Clouds, right background: Microwave Radiometer Humidity and Temperature Profiler (Hatpro); d) PARSIVEL laser-disdrometer; e) Micro Rain Radar (Instruments in a) - e) located in Ny-Ålesund, Svalbard) f) Particle Imaging Package video-disdrometer (located in Hyytiälä, Finland).

4.1 Surface measurements

Observations of an instrument that are directly made within its vicinity are called in situ. The instrumentation does not necessarily mean to be ground-based but in the following a classical precipitation gauge is used as in situ instrument at the surface. Other surface measurement systems are different disdrometers, which are also important for precipitation observations.

4.1.1 Particle Imaging Package

The Particle Imaging Package (PIP, Figure 4.1f) is a video-disdrometer from the National Aeronautics and Space Administration installed at the measurement site in Hyytiälä, Finland. It is the successor of the Snow Video Imager (*Newman* et al.,

2009) with an improved camera and software (*Tiira* et al., 2016), but the principle stays the same. PIP has a charge-coupled device camera with a frame rate as high as 380 frames per second directed towards a 2 m distant light source (*Tiira* et al., 2016) of a 300 W halogen flood lamp (*Newman* et al., 2009). The measurement volume is defined by the field of view (48 × 64 mm) and the depth of field (2 m). Particles falling through the volume between light and camera are recorded and a 2D-grayscaled video image is saved. From the particle shadow on the image with a resolution of 0.1 × 0.1 mm, the area-equivalent diameter is measured (*Newman* et al., 2009). The latter ranges from 0.125 mm to 25.875 mm divided into 105 bins, whereas the last bin includes every particle with diameter larger than 25.875 mm (*von Lerber* et al., 2017). Due to the observation of consecutive frames and the high frame rate the fall velocity (v(D)) of a single particle can be derived. From v(D) a particle size distribution (PSD) is derived for every minute. The estimated error of the particle size is 18% (*Newman* et al., 2009).

4.1.2 Parsivel

PARSIVEL (which stands for "PARticle SIze VELocity", Figure 4.1d) is an optical laser-disdrometer produced by the manufacturer OTT. The laser transmits a flat laser sheet at 650 nm with an area of 27 × 180 mm and a height of 1 mm (*Battaglia* et al., 2010). The principle of this instrument is a voltage decrease which occurs when the laser sheet is blocked by particles falling between transmitter and receiver. The fall velocity is measured via the time delay of the particle intercepting the laser beam. Particle size is proportional to the amplitude of the voltage decrease. Within PARSIVEL's retrieval rationale measured particles are assumed to be raindrop-like, thus, assumed to be spherical (*Battaglia* et al., 2010). The output diameter is a volume equivalent sphere diameter, which is only valid for rain particles. When snow is measured, an uncertainty of the dimension of the particle has to be considered. After the determination of the dimension and fall speed, the particles are divided into 32 available size classes ranging from 0.062 mm to 24.5 mm, although the registration usually begins at the size of 0.25 mm (*OTT*, 2016b). Another 32 classes are used to divide velocity in non-equidistant ranges between 0.05 and 22.4 m s^{-1}. Temporal resolution is 1 minute. PARSIVEL's software provides the user with a PSD as well as a velocity distribution, from which a hydrometeor type classification is given. The latter distinguishes between eight different precipitation types (drizzle, drizzle+rain, rain, rain/drizzle+snow, snow, snow grains, soft hail, hail). Furthermore, PARSIVEL provides the variables: accumulation of liquid water [mm], rain intensity (rate) [mm/h], and an internally calculated estimate of radar reflectivity

[dBZ]. Rain rate is indicated with an uncertainty of $\pm$ 20% for solid precipitation (*OTT*, 2016b). Beyond this uncertainty for rain rate, *Battaglia* et al. (2010) have investigated PARSIVEL's ability to measure falling snow in more detail: Their conclusion was an underestimation of fall velocity for small snow particles and an overestimation for large particles with up to 30% - 40% uncertainty. PARSIVEL's software assumes a certain relationship between the dimensions of a particle in the horizontal and vertical direction, matching the size of a rain drop. This assumption fails when measuring snow particle's size and fall velocity and these uncertainties propagate into the PSD retrieval of the instrument.

The differences between the video-disdrometer PIP and the laser-disdrometer PARSIVEL are the different detection principles of using images of the high resolution camera and the physical voltage drop of a laser beam, respectively. Whereas for PIP the light is only a source to illuminate the volume to get a better contrast for the gray-scaling image, PARSIVEL uses the power of the laser for detection.

4.1.3   Precipitation gauge

A precipitation gauge can be used for observing both, liquid and solid precipitation, but the latter is always melted and provided as the water equivalent value. Thus, the phase distinction has to be made via temperature and can not be directly obtained from the gauge measurements.

There are different kinds of gauges, such as volumetric, heated tipping-bucket or weighing gauges and they all suffer from different uncertainties. In this study, an automated weighing gauge manufactured by OTT with an orifice of 400 cm^2 is used: Pluvio2 L 400 (Figure 4.1a, further only called Pluvio). The principle is like its name already implies: precipitation falls into the bucket and is weighed by a sensitive scale every minute. The variables measured by this gauge are precipitation intensity (or precipitation rate) [mm/h] with an absolute (and relative) accuracy of $\pm$ 0.1 mm ($\pm$ 1%) and different accumulated precipitation values from which the non-real time accumulation [mm] is used, with a threshold of 0.05 mm and the same just stated absolute and relative accuracy as for the precipitation intensity (*OTT*, 2016a).

Gauges are very prone to underestimation of solid precipitation due to high wind, or overestimation due to blowing snow. Therefore, different wind shieldings have been designed, used and tested in the last decades to limit the uncertainty of gauge measurements which can be up to 50% (*Rasmussen* et al., 2012).

The Pluvio in Ny-Ålesund, which is used for accumulation observations compared to calculated snowfall accumulation from radar measurements (Section 6), is surrounded by a single Alter wind shield. As mentioned in the Introduction the WMO

has organized a Solid Precipitation Intercomparison Experiment (SPICE, between 2012-2015; *Nitu* et al., 2018), from which different correction (transfer) functions for estimating the wind effect around gauges have emerged. Within this thesis two correction functions have been applied.

For gauges with a single Alter windshield *Kochendorfer* et al. (2017, hereafter K17) developed two different universally applicable functions for liquid (not used in this work) and mixed/solid precipitation

$$CE = a \cdot exp(-b \cdot U) + c, \tag{11}$$

with CE for Catch Efficiency (dimensionless), using eight measurement sites for testing. Both transfer functions depend on wind speed at gauge height (U). Surface temperature (T_{air}) directly influences the equation for liquid precipitation (not needed here), but only indirectly Eq. (11). For each function, the three parameters: a, b and c, are needed. They have been empirically derived and are different for mixed and solid (Table 3, K17). The assumed true precipitation amount is calculated by dividing the observed precipitation amount by the calculated CE-value. It is corrected to always be above or equal to 1. K17 defined two temperature ranges to differentiate which set of parameters, for liquid, mixed or solid, has to be used. Liquid precipitation is assumed for $T_{air} > 2°C$, mixed precipitation is assumed for $2°C \leq T_{air} \leq -2°C$ and solid is assumed if the air temperatures are below -2°C.

Wolff et al. (2015, hereafter W15) have developed a correction function particularly for a site in Norway. This site is surrounded by mountains and thus might be better comparable to the site in Ny-Ålesund. In contrast to K17, W15 only use one function for all precipitation types with constant parameters and not only in dependency of wind speed, but also temperature (see Eq. (13) in W15).

4.2   Radar

To gain information on the atmosphere from low to high altitudes, remote sensing instruments are used. They can be located on the ground, on an aircraft or in space. There are active and passive operating instruments. In this work, the focus is on the active instruments, on RAdio Detective And Ranging (long for: radar), as these are usually used to retrieve snowfall rates.

The main principle is based on transmitted electromagnetic waves into the atmosphere and received backscattered signals from targets such as precipitation or cloud particles, aerosols or also unwanted targets such as insects. The backscattered signal is dependent on the used wavelength, the size of the particle in respect to the

wavelength and on dielectric properties of the particle. With the time difference between outgoing and incoming signal the distance to the target can be determined. A radar can be characterized by its frequency, the corresponding wavelength or with a certain alphabetic character plus the suffix '-Band', that historically has been assigned to frequency ranges. Weather radars (S-, C-, X-Band) measure at lower frequency (3, 5.5, 10 GHz), thus larger wavelengths (10, 5.5, 3 cm), to typically gain information about the spatial distribution of hydrometeors in the atmosphere. These information result in the application of for example QPE, nowcasting, or storm tracking. As the used wavelength of weather radars is much larger than the diameter of observed rain drops or snowflakes, the backscattered signal is usually assumed to be in Rayleigh scattering regime.

When talking about millimeter-wavelength radars (usually Ka-, W-Band with 8.6 mm and 3.19 mm, respectively), they are also called cloud radars. The sensitivity of higher radar frequency is higher towards smaller particles. Cloud particles are usually of the size of 5 - 25 μm (*Lohmann* et al., 2016), thus, Rayleigh approximation is valid. Within the last decade cloud radars were also used for investigating especially solid precipitation, to better understand their microphysical properties (*Matrosov* et al., 2008; *Kulie and Bennartz*, 2009; *Levizzani* et al., 2011; *Leinonen* et al., 2012; *Tecla Falconi* et al., 2018). Regarding the broad size range of solid precipitation (ice crystals and snowflakes) from 0.01 mm up to 10 cm (*Lohmann* et al., 2016), the wavelength is likely to be of about the same size as the observed particles. As a result, the measurements are within the much more complex Mie scattering regime. The quantity that radars utilize to describe the measured power is the radar equivalent reflectivity factor Z_e. A general equation to calculate radar reflectivity by assuming small spherical particles is defined as (*Bringi and Chandrasekar*, 2001)

$$Z = \int_D D^6 N(D) dD \qquad (12)$$

with Z in the units of mm^6/m^3, thus diameter D in millimeter and N(D)dD is the number of spheres per cubic meter. It is common to express Z in the logarithmic units of dBZ (10 $\log_{10}$(Z)), as the range of particle sizes and amounts are wide.

Considering Mie scattering, the Rayleigh scattering approximation (assuming spherical particles) is not valid anymore and an equivalent radar reflectivity is used to describe any kind of particle shape (*Bringi and Chandrasekar*, 2001)

$$Z_e = \frac{\lambda^4}{\pi^5 |K|^2} \int_D \sigma_b(D) \, N(D) \, dD \qquad (13)$$

with the wavelength λ [mm], the unitless dielectric factor $|K|^2$ which is different for water or ice and also wavelength dependent, the backscatter cross section σ_b [mm^2] and the particle size distribution N [m^{-4}], both as a function of the diameter of the observed particle. The integral is generally determined over a certain diameter interval [m] with the typical limits of minimum and maximum observed particle diameter. Z_e has the same unit as Z and is often given in the dB expression.

The two radars used in the snowfall rate retrieval application of Ny-Ålesund data (Section 6), both, are a vertically pointed frequency modulated continuous wave (FM-CW) Doppler radar. Other instrument specific information can be found in the following sections.

4.2.1 Microwave Radar for Arctic Clouds

The active part of the Microwave Radar for Arctic Clouds (MiRAC-a, for simplicity in this thesis it is only referred to as MiRAC, Figure 4.1b and 4.1c, left) is a W-Band radar, operating at a wavelength of λ = 3.19 mm (f = 94 GHz). There is also a passive part, which is a microwave radiometer operating at 89 GHz; this part of the instrument will not be further described or used. However, another radiometer, the humidity and temperature profiler (HATPRO, Figure 4.1c, right), is used to retrieve the amount of liquid water in an atmospheric column: liquid water path (LWP). The latter is derived from measured brightness temperatures at a range of K-Band frequencies (22.24-31.4 GHz *Nomokonova* et al., 2019). The temporal resolution is 1-2 s. The accuracy of HATPRO measurements for LWP is within 20-25 g/m^2 (*Rose* et al., 2005). These LWP measurements are later relevant for a detailed evaluation of the snowfall rate retrieval application in Section 6.

The W-Band radar MiRAC has a very low transmitter power consumption of 1.5 W. The separation into one transmitting and one receiving antenna (receiving the active and passive part) allows the continuous wave transmission and the receiving antenna is protected from saturation (*Küchler* et al., 2017). A strong blower ensures the precipitation free antenna surface.

The available height range starts at 102 m and can reach up to 12 km. In this work, the height range between 120 and 180 m is used with an interval of 3.2 m. The time sampling is at a rate of 3 s and in this worked averaged to 1-minute values. From the measured power variables such as for example the equivalent radar reflectivity, Doppler spectra, Doppler velocity and spectral width are derived. For this work, Z_e is the variable of interest. Its uncertainty is in the order of 0.5 dBZ and the general sensitivity in the range of -65 to -45 dBZ (*Mech* et al., in review, 2019). The beam

width is 0.48 degree.

Originally designed for cloud observations, millimeter-wavelength radars have shown a good ability to be used for precipitation as well (*Kollias* et al., 2007). Moreover, for solid precipitation, especially dry snowfall, attenuation at W-Band is small compared to radars operating at higher wavelengths (*Matrosov* et al., 2008).

4.2.2 Micro Rain Radar

The Micro Rain Radar (MRR, Figure 4.1e) operates at a wavelength of $\lambda = 12.38$ mm (f = 24 GHz), the so called K-Band. Compared to (pulsed) radars in the same frequency range, MRR has a low power consumption of 25 W. If the installed dish heater is turned on, a consumption of 500 W is added. The heating system prevents snow accumulation on the parabolic offset dish antenna, which has an effective aperture diameter of 0.5 m.

Starting at the lowest range bin of 30 m, MRR has a maximum height detection of 870 m with interval steps of 30 m. As the lower radar range bins usually suffer from noisy signals, but for this work information lowest as possible are needed for surface comparisons, the 4th - 6th range bins are used. Reflectivity values are thus averaged over the heights of 120 to 180 metres. The temporal resolution is as high as 10 s, but is internally averaged to 1 minute values for the output. The beam width of the signal is 1.5 degree. Equivalent radar reflectivity, Doppler velocity and Doppler spectra are some of the products of the instrument.

As the name already implies, this radar (and its software) was originally built to measure liquid precipitation. *Maahn and Kollias* (2012) developed an Improved MRR Processing Tool (IMProToo) for better snow observations, through dealiasing the Doppler spectra and removing noisy signal. The lowest sensitivity value decreases from -5 dBZ for Metek's standard analysing method to -8 dBZ from a method by *Kneifel* et al. (2011b) to -14 dBZ for the new proposed method by *Maahn and Kollias* (2012). Within this work these improved variables are used.

4.2.3 Radar cross section simulations

For the snowfall rate retrieval in Section 5, the radar reflectivity is not used from observations, but calculated with Eq. (13) for the two corresponding radar wavelengths of 12.38 mm (K-Band) and 3.19 mm (W-Band). For each, the dielectric constant is different, thus $|K|^2 = 0.92$ ($|K|^2 \approx 0.76$) for K-Band (W-Band) are used. N(D) can either be used from the PIP measurement or as it is done in the snowfall rate retrieval, approximated with the exponential function of Eq. (3).

The unknown quantity radar backscattering cross section σ_b can be computed with

two different scattering methods: TMM and DDA (Section 2.5.2). A ready-to-use python package for the TMM (*Leinonen*, 2018) is applied for both, K- and W-Band, together with a dataset of snow event measurements (*Moisseev*, 2018) to calculate σ_b in dependency of the volume equivalent diameter and time. Additionally, for W-Band the DDA scattering model for more complex shaped particles is utilized. For this, a combination of three datasets are used as input for the DDA calculation: aggregated snowflakes (different sizes of dendrites, needles, plates, bullet rosettes, spheroidal crystals, short: aggregates) (*Leinonen and Moisseev*, 2015), aggregates and crystal snowflakes at different riming stages and with three growth scenarios (*Leinonen and Szyrmer*, 2015) and aggregates as well as fractals of snowflakes (*Tyynelä* et al., 2011).
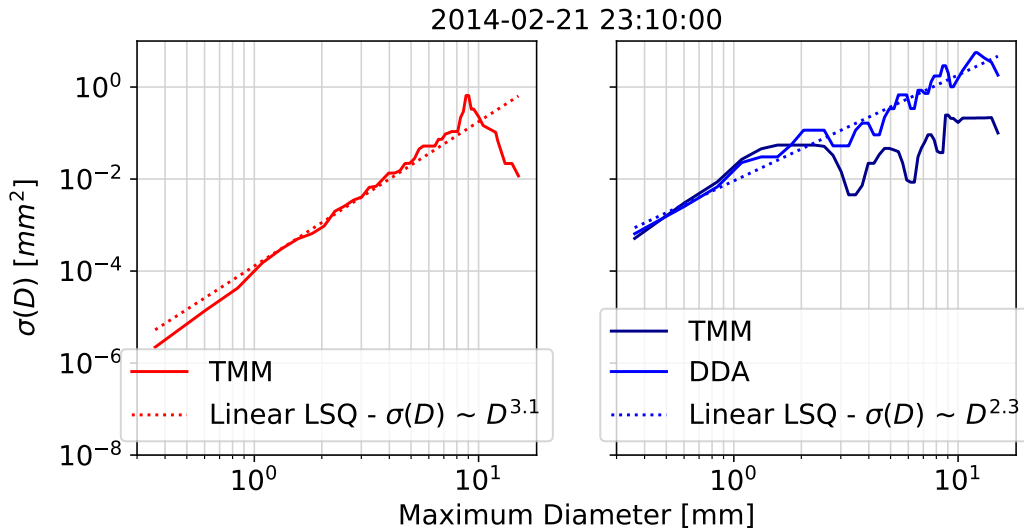
Figure 4.2: Radar backscattering cross section (σ(D)) against diameters of snow particles measured with PIP in Hyytiälä, Finland on February 21st 2014 23:10 UTC. Simulated σ(D) with T-Matrix Method (TMM) for K-Band (left) and simulation with TMM and Discrete Dipole Approximation (DDA) for W-Band (right) are displayed in log-log space. For both σ(D) a line with the linear least-squares approach is fitted, approximating σ(D) with a power law.

The computation results of the backscatter cross section in the unit of mm^2 are shown in Figure 4.2, plotted against the maximum diameter [mm] for the 21st February of 2014 at 23:10 UTC. For smaller diameter (up to 10 mm) σ_b follows an approximately linear line for K-Band, which indicates that the particles follow the Rayleigh approximation well. For larger particles, diameters as large as the size of the wavelength, Mie or Resonance regime is approached. In W-Band the resonance effects due to the Mie regime are even more pronounced, already for smaller diameters. Especially for TMM calculations a deviation from a linear line can be noticed, which can lead to an underestimation of σ_b by a factor of 50-100 *Tyynelä*

et al. (2011). For this reason, DDA calculations were done as well. With this scattering method the snow particles are represented better for higher frequencies.

A linear least square fit approximates the backscatter cross section with a power law $\sigma_b = \alpha\, D^\gamma$. Within this snapshot in Figure 4.2, the exponent γ is close to 3 (2) for K-Band (W-Band). However, plotting all available time steps in a histogram of the exponent γ for both wavelengths, a maximum value in K-Band of $\gamma \approx 4$ is obtained (Figure 4.3), thus having a proportionality of $\sigma_b \propto D^4$. For W-Band the same procedure gives a dependency of $\gamma \approx 2$ (Appendix, Figure A.1), thus $\sigma_b \propto D^2$. Within Rayleigh regime, it can be assumed that the radar cross section is proportional to m^2 (e.g. *Matrosov* et al., 2009). And, as the mass of a snowflake is less ambiguous to determine than its diameter, the radar cross section simulations have been also set in the dependency of mass (not shown), which for K-Band turns out to still follow the Rayleigh approximation with its proportionality to $\sim$m^2. For W-Band the backscatter cross section seems to be directly related to the mass which in turn connects the W-Band reflectivity (Z$_{e,W}$ directly to the ice water content (IWC, mass per cubic meter). The snowfall rate S is already proportional to the mass (Eq. (9)). Thus, the linear correlation of Z$_{e,W} \propto$ m $\propto$ IWC and thus also Z$_{e,W} \propto$ S, is taken as the basis and confirmation that W-Band reflectivities can very well be used for a snowfall rate retrieval.
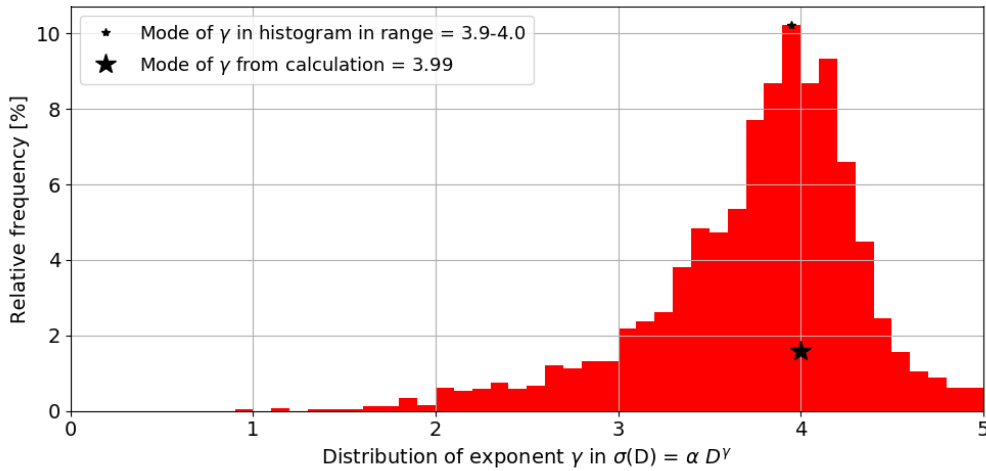
Figure 4.3: The distribution of the exponent γ from the power-law $\sigma(D) = \alpha\, D^\gamma$. Variable D is the snow particle dimension. The backscatter cross section ($\sigma(D)$) is simulated with the T-Matrix Method for the wavelength $\lambda = 12.38$ mm. For the latter mass and snow particle diameter are used from a dataset of 5-minute snow measurements for two consecutive winters 2014/2015 in Hyytiälä, Finland. The distribution values result from a polynomial fit from which the calculated mode value with two decimal places is calculated and displayed with a large black star. The histogram bin range is 0.1 and the histogram mode value is shown with a small black star.

Table 4.1: Summary over used instruments and models in Hyytiälä and Ny-Ålesund to see which variables have been measured and/or derived or have been used as input for the models. LM15: *Leinonen and Moisseev* (2015), LS15: *Leinonen and Szyrmer* (2015), T11: *Tyynelä* et al. (2011).

	instrument	forward model	measured	input	derived
Hyytiälä	PIP		D_{PIP} $v_{PIP}(D)$		$m(D)$
			$N_{PIP}(D)$		$N_0 \to N(D)$
		TMM		D_{PIP} $m(D)$	$\sigma_{b,\ K,TMM}$
					$\sigma_{b,\ W,TMM}$
		DDA		LM15 / LS15 / T11 — D_{max} $m(D)$	$\sigma_{b,\ W,DDA}$
Ny-Ålesund	PARSIVEL		D_{PAR}		$m(D)$
			$N_{PAR}(D)$		$N_0 \to N(D)$
	MRR		$Z_{e,MRR}$		
	MiRAC		$Z_{e,MiRAC}$		

5 Development of a snowfall rate retrieval

With two different methods Z_e-S relationships are derived from PIP measurements and simulations of backscatter cross sections for K-Band and W-Band radar reflectivities at the station in Hyytiälä, Finland. In the following sections these methods are described in detail. Additionally, an uncertainty assessment is performed and analysed, to determine the best relationship for each reflectivity simulation.

5.1 Derivation of the Z_e-S relationship parameters

It has been historically evolved to write the Z_e-S power law: reflectivity as a function of snowfall rate, although the variable of interest is the snowfall rate to be calculated from radar-measured reflectivity values. Thus, in this section the rearranged Equation (10) solved for S [mm/h], is used:

$$S = (\frac{1}{a_{zs}} Z_e)^{\frac{1}{b_{zs}}} \tag{14}$$

The prefactor a_{zs} and the exponent b_{zs} are needed to determine the snowfall rate S. These two parameters are derived within the following snowfall rate retrieval procedure. The parameter b_{zs} is unitless and a_{zs} has the unit of $mm^{6-b_{zs}}$ $h^{b_{zs}}$ m^{-3}.
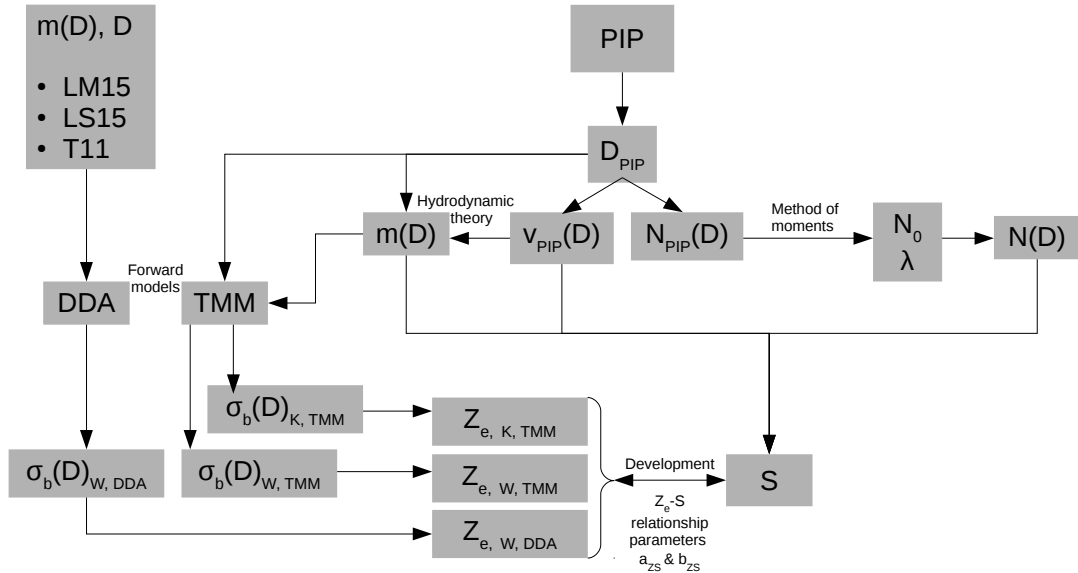
Figure 5.1: Overview scheme of measured, calculated and simulated variables needed for the development of the parameters for the Z_e-S relationship.

For the calculations of S and Z_e a dataset from PIP measurements is used with selected snow events, consisting of the variables: velocity $(v_{PIP}(D,t))$, PSD $(N_{PIP}(D,t))$ and mass $(m(D,t))$. In total 3012 5-minute time steps are available from two winters

of 2014/2015. For this dataset only events with temperatures below 0°C were used. A further restriction excluded events that were close to 0°C during the whole time of the event, to account for solid particles only (*von Lerber* et al., 2017). Whereas $v_{\text{PIP}}(D,t)$ and $N_{\text{PIP}}(D,t)$ have been a direct output from PIP, $m(D,t)$ has been calculated with hydrodynamic theory by courtesy of *von Lerber* et al. (2017).

For the snowfall rate retrieval development the PSD from PIP is approximated with the exponential function (Eq. (3)), to account for a continuous size distribution. For the derivation of the exponential PSD (further just called $N(D,t)$), the intercept parameter $N_0(t)$ and the slope $\Lambda(t)$ are calculated with the method of moments (Section 2.3), which used $N_{\text{PIP}}(D,t)$ as input for the moment calculation (Eq. 4). $Z_e(t)$ is then calculated with Eq. (13) with $N(D,t)$ and $\sigma(D,t)$. The latter is simulated with two different scattering methods (Section 2.5.2), for K- and W-Band, respectively (Section 4.2.3).

An overview scheme can be found in Figure 5.1, in which the origin of all used (measured, calculated and simulated) variables needed to calculated Z_e and S to retrieve the parameters for the Z_e-S relationship are displayed.
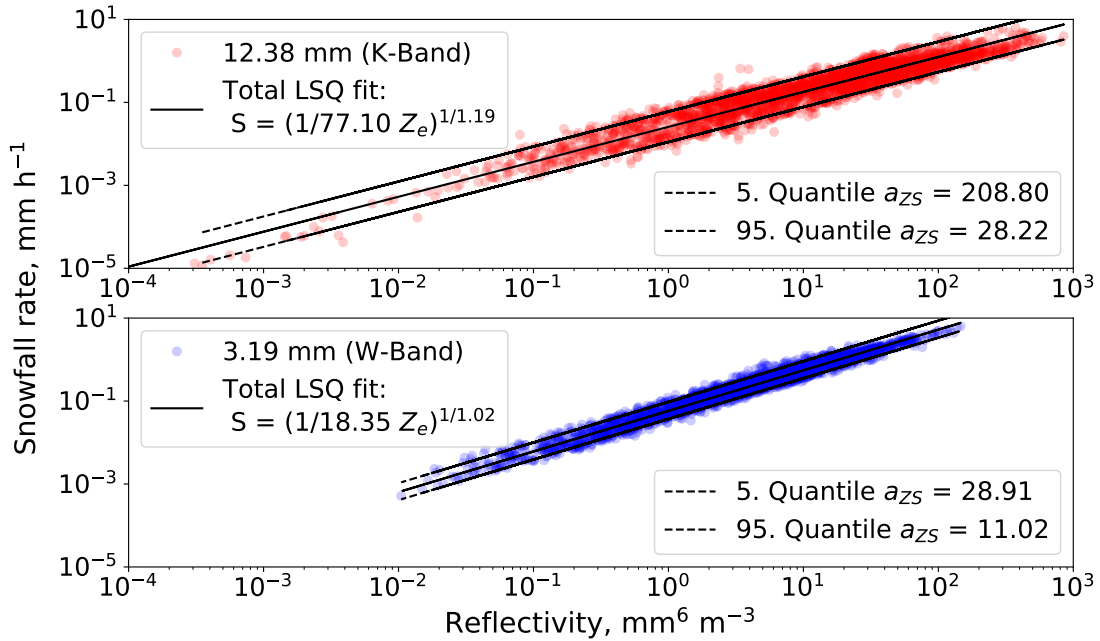
Figure 5.2: The average S-Z_e relationship: Scatterplot of calculated snowfall rate and reflectivity from PIP measurements and radar cross section simulations for K- (above) & W-Band (below). A total least squares (TLS) fit is the solid black line. The dashed black lines use the same exponent of the TLS fit but are the 5. & 95. Quantile of all available points, to give the minimum and maximum prefactor a_{zs}.

Method 1: the average Z_e-S relationship. For this first method the calculated reflectivity (Eq. (13)) is plotted against the calculated snowfall rate (Eq. (9)) with logarithmic scales for all available time steps. The scatter plot in Figure 5.2 shows

the results for K-Band and W-Band. For the exponent and prefactor derivation, a total least squares fit is calculated, to account for both, the uncertainty in S and Z_e. For K-Band (W-Band) the parameters $a_{zs} = 77.10$ (18.35) and $b_{zs} = 1.19$ (1.02) are obtained. Similar to *von Lerber* et al. (2017) another fit to get the 5. and 95. quantile of the prefactor was derived, for this, the exponent is kept as a constant. The value range of $28.22 \leq a_{zs} \leq 208.8$ for K-Band ($11.02 \leq a_{zs} \leq 28.91$ for W-Band) shows the wide variation of a_{zs} values, especially for K-Band. Looking at one single Z_e value one gets different S values in the order of a magnitude (e. g. for $Z_e = 10^{-1}$ mm^6 m^{-3} the range in S can be from 10^{-3} mm h$^{-1} \leq S \leq 10^{-2}$ mm h^{-1}).

Method 2: the analytical Z_e-S relationship. Following *von Lerber* et al. (2017), method 2 considers the time-dependency of the parameters and provides an instantaneous Z_e-S relationship for each time step. For a better readability, the time dependency of each variable is omitted in the following equations.

The analysis begins with rewriting Eq. (9) and (13) with the approximations of each function (Eq. (1 - 3)) and $\sigma_b(D) = a_m \, D_m^{\,b}$. The second step is the integration over an infinite diameter size on which the complete Gamma function (Eq. (5)) can be applied. With these steps the snowfall rate then becomes

$$
\begin{aligned}
S &= \frac{1}{\rho_w} \int_0^\infty m(D)\, v(D)\, N(D)\, dD \\
&= \frac{1}{\rho_w} \int_0^\infty a_m \, D^{b_m} \, a_v \, D^{b_v} \, N_0 \, exp(-\Lambda\, D)\, dD \\
&= \frac{1}{\rho_w} \, a_m \, a_v \, N_0 \, \Lambda^{-(b_m + b_v + 1)} \, \Gamma(b_m + b_v + 1).
\end{aligned}
\tag{15}
$$

Following the previous mentioned steps, the reflectivity factor can be written as

$$
\begin{aligned}
Z_e &= \frac{\lambda^4}{\pi^5 \, |K|^2} \int_0^\infty \sigma_b(D)\, N(D)\, dD \\
&= \frac{\lambda^4}{\pi^5 \, |K|^2} \int_0^\infty a_\sigma \, D^{b_\sigma} \, N_0 \, exp(-\Lambda\, D)\, dD \\
&= \frac{\lambda^4}{\pi^5 \, |K|^2} \, a_\sigma \, N_0 \, \Lambda^{-(b_\sigma + 1)} \, \Gamma(b_\sigma + 1).
\end{aligned}
\tag{16}
$$

Inserting Eq. (15) and (16) into the Z_e-S relationship (Eq. (10)) the analytical solution for the two parameters in dependency of time is obtained (not shown). Whereas the exponent b_{zs} simply reduces to

$$
b_{zs} = \frac{b_\sigma + 1}{b_m + b_v + 1},
\tag{17}
$$

the prefactor a_{zs} is much more complex. Its dependency is on all parameters of the m(D,t), v(D,t) and N(D,t) relationships (Eq. (6) in *von Lerber* et al., 2018)). In accordance with *Rasmussen* et al. (2003), *von Lerber* et al. (2017) have found that the strongest dependency is due to the intercept parameter N_0. The parameters b_m and b_σ for the calculation of b_{zs} (Eq. (17)) are calculated from polynomial fits in log space to obtain power laws for m(D,t) and σ(D,t). For b_v the value 0.2 is used, taken from the evaluation of *Tiira* et al. (2016). As the exponent b_{zs} is a function of time, a mean over all time steps is calculated to get a fixed parameter for K-Band (W-Band): b_{zs} = 1.48 (= 1.14). With this mean value for b_{zs} and the calculated snowfall rate and reflectivity values from Method 1, Eq. (14) can be solved for the parameter a_{zs} for each time step. N_0(t) is calculated from the method of moments (Eq. (8), Section 2) and as a result, Figure 5.3 shows the prefactor as a function of the intercept parameter N_0(t), for better readability, displayed in logarithm to the base of 10: $\log_{10}(N_0(t))$. Especially for K-Band a large spread for $a_{zs}(N_0(t))$ in the order of 10^3 is seen. The large scatter for lower N_0(t) values reduces towards larger N_0(t) values. W-Band does not show a large dependency towards N_0(t) (note the reduced y-Axis range of one order of magnitude). For both, a linear least square fit approximates a power law for $a_{zs}(N_0(t))$, further called $a_{N_0,\text{fit}}$.
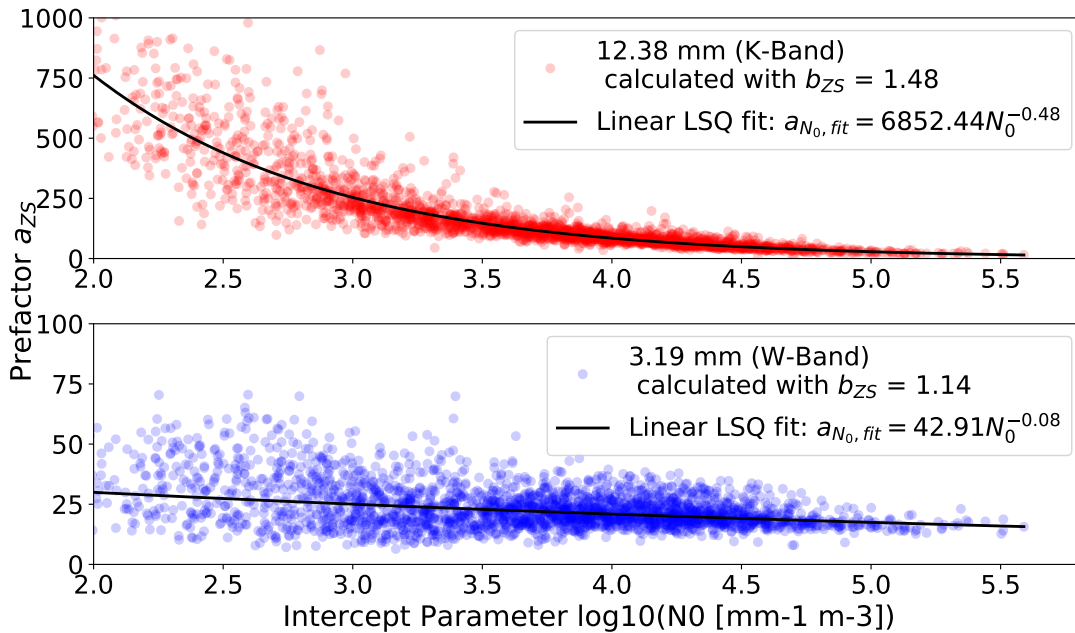
Figure 5.3: Prefactor a_{zs}, calculated by solving Eq. (14) for a_{zs} using a mean value of b_{zs} from Eq. (17), in dependency of intercept parameter N_0. K-Band (red, top) and W-Band (blue, bottom). For better readability, the x-Axis is displayed in logarithm to the base of 10. The solid black line in each panel is a linear least-squares fit.

5.2   Uncertainty analysis

To check how method 1 and method 2 compare to each other, an uncertainty analysis is performed. Different RMSE values are calculated in the dependency of a range of $\log_{10}(N_0(t))$ values from $2 \leq \log_{10}(N_0(t) \leq 5$ [mm^{-1} m^{-3}] with an interval of 0.1 mm^{-1} m^{-3}. The truncation on the left considers the minimum available total amount of particles within the PSD. The upper limit sets a limit for a maximum amount and reduces the number of outliers. The variables $Z_e(t)$, $S(t)$, $a_{zs}(N_0(t))$, and $a_{N_0,\text{fit}}$ are sorted by their times for each $\log_{10}N_0(t)$ interval.

To calculate the RMSE of S with the average parameters, method 1, the calculated snowfall rates from PIP measurements are assumed to be the truth. Then, for each $\log_{10}N_0(t)$ interval step the snowfall rate is determined anew with the parameters of method 1 and finally, the RMSE can be determined.

The RMSE for method 2 is the total RMSE, a combination of the RMSE from the prefactor and the RMSE from the reflectivity. For the error in S due to a_{zs} (Δ S_a) the fitted power law $a_{N_0,\text{fit}}$ is used to calculate the assumed true snowfall rate. The instantaneous $a_{zs}(N_0(t))$ values are used for the estimated snowfall rate. As the exponent b_{zs} is set as a constant value, the error is neglected. However, $a_{zs}(N_0(t))$ gets another uncertainty from the simulated reflectivity. The RMSE due to Z_e (ΔS_{Z_e}) propagates into the total RMSE of method 2. For ΔS_{Z_e} a Gaussian distribution with the mean at 0 dBZ and a standard deviation of 1 dBZ is assumed. Drawing random values from this distribution and perturbing the reflectivity with this ΔZ_e, a new S can be calculated and a RMSE due to the reflectivity is derived. With $\Delta S = \sqrt{\Delta S_a^2 + \Delta S_{Z_e}^2}$, the total RMSE for method 2 can be determined.

Figure 5.4 displays the results of the uncertainty analysis. For K-Band, method 1 has the highest RMSE of 0.55 mm/h at a $\log_{10}(N_0)$ value of around 3.5 mm^{-1} m^{-3}. For higher $\log_{10}(N_0)$ values the uncertainty in S increases to 0.87 mm/h. Method 2 has a significantly smaller RMSE along the whole $\log_{10}(N_0)$ interval. Up to a value of 4.2 mm^{-1} m^{-3} the RMSE stays below 0.21 mm/h and also at higher interval values it is highest at 0.3 mm/h. The mean value over the whole interval for method 1 is around 0.344 mm/h.

As the second method consists of a random changing error in Z_e, a simple mean would not suffice. Thus, a set of 100 runs is performed to calculate the total RMSE from which then a first order polynomial regression leads to the RMSE function of $\log_{10}(N_0)$:

$$RMSE(log_{10}(N_0)) = p_1 \, log_{10}(N_0) + p_2. \tag{18}$$

For K-Band the parameters are $p_1 = 0.083$ and $p_2 = $ -0.142. The range of uncertainty
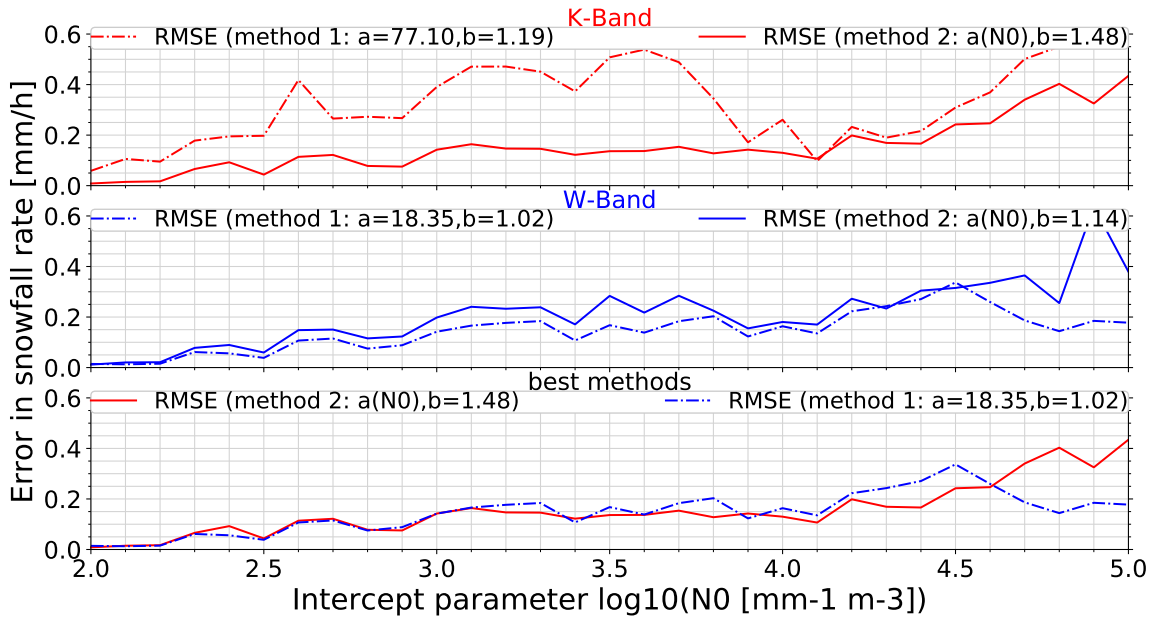
Figure 5.4: Uncertainty in snowfall rate (S) for K-Band (top), W-Band (middle) and both methods with the smallest uncertainty, respectively (bottom). Method 1 with the average parameters (solid line) and method 2 with analytically calculated parameters (dash-dotted line).

with this equation starts at 0.023 mm/h for $\log_{10}(N_0)$ of 2 and has its maximum at a RMSE of 0.274 mm/h for $\log_{10}(N_0) = 5$. The mean value of this linear function is 0.149 mm/h.

For W-Band both methods result in a RMSE below 0.4 mm/h almost along the whole range. The RMSE of method 2 is almost over the whole range around 0.05 mm/h larger than the RMSE values of method 1. Calculating the mean over the whole interval for method 1 gives a value of 0.145 mm/h. For the RMSE function, the parameters can be found in Table 5.1.

Comparing the uncertainty values of method 2 of K-Band and method 1 of W-Band by overlaying them in the same plot (Figure 5.4, bottom) they agree pretty well, especially for the lower $\log_{10}(N_0)$ intervals.

On the basis of this uncertainty analysis it is determined which method to use for the further snowfall rate retrieval application in Section 6: method 2 is the best method to use for K-Band and method 1 for W-Band. For K-Band the Z_e-S relationship is significantly improved by setting the prefactor in the dependency of the intercept parameter N_0. The average relationship of method 1 for W-Band already shows a small uncertainty in S. In Table 5.1 the results for the different Z_e-S relationship parameters are summerized. The highlighted cells are the parameters, which will further be used in the next section.

Table 5.1: Overview table of calculated parameters a_{zs} and b_{zs} from 2 different methods deriving the Z_e-S relationship and the uncertainty in S for 2 radar wavelength bands. The grey shading highlights the best parameters used for an evaluation when applying to measured reflectivity values.

	a_{zs} [mm$^{6-b_{zs}}$ h$^{b_{zs}}$ m^{-3}]	b_{zs}	S_{RMSE} mean [mm/h]	$S_{RMSE}(\log_{10}(N_0))$ [mm/h]
K-Band	85.65	1.19	0.345	-
	$a(N_0) = 7612.9\ N_0^{-0.48}$	1.48	0.149	0.023 to 0.274 = 0.083 $\log_{10}(N_0)$ - 0.142
W-Band	18.35	1.02	0.145	-
	$a(N_0) = 49.91\ N_0^{-0.08}$	1.14	0.201	0.05 to 0.351 = 0.1 $\log_{10}(N_0)$ - 0.078

6 Application of the snowfall rate retrieval

To evaluate whether the derived Z_e-S relationship from the data in Hyytiälä, Finland, could also be applied to a different location, in fact, the Arctic, the newly developed parameters are applied to the radar measurements at the site in Ny-Ålesund. The calculated radar-based derived snowfall rates are set into the context of other meteorological measurements and further compared to surface observations from Pluvio. Possible uncertainties in the retrieval procedure and its application to measurements are discussed in Section 6.2.

6.1 Case studies

In the following sections, five case studies demonstrate the application of the Z_e-S relationship for K-Band radar MRR (Section 4.2.2) and W-Band radar MiRAC (Section 4.2.1). As the intercept parameter of the PSD is needed for the application of the K-Band Z_e-S relationship, the PSD of PARSIVEL measurements (Section 4.1.2) is used to calculate the exponential PSD with the method of moments for N_0 and Λ (Section 2.3). The used parameters a_{zs} and b_{zs} are highlighted in Table 5.1, the prefactor value range (maximum and minimum value) for the MRR Z_e-S relationship for each case study are summarized in the Appendix in Table A. The applied uncertainty for the calculated snowfall rate for MiRAC is 0.15 mm/h and for MRR the value range is also given in Table A for each case study.

The determination of snow events at Ny-Ålesund was initially done by checking the hydrometeor type classification product from PARSIVEL for snow. This classification can be found in a Quicklook Browser[3] of the UoC, when choosing "Parsivel_Overview" from the select button. If a day depicted *snow*, other meteorological values such as relative humidity, temperature, wind speed and liquid water path were investigated. From this first broad selection by hand the following case studies are investigated in more detail.

6.1.1 Case study 1: 2018-01-27

On January 27th clouds appeared over Ny-Ålesund around 8:00 UTC, which can be seen in the reflectivity values of the cloud radar MiRAC displayed in a time-height series for the whole day and up to 10 km height in the Appendix Figure A.2, in which cloud properties and precipitation are detectable (for comparison, MRR reflectivities are shown as well for the height range up to 870 m). Higher MiRAC reflectivities after noon and PARSIVEL's hydrometeor classification (see Quicklook

---

[3]http://gop.meteo.uni-koeln.de/~Hatpro/dataBrowser/dataBrowser4.html?site=Ny-Alesund

Browser[4]) indicate light solid precipitation. Only during the evening a more pronounced precipitation was measured and thus, the case study event is restricted from 19:00 to 23:00 UTC.

As a first step, only reflectivity values and the calculated snowfall rates with the Z_e-S relationships from the corresponding parameters of Table 5.1 for MRR ($Z_{e,MRR}$, S_{MRR}) and MiRAC ($Z_{e,MiRAC}$, S_{MiRAC}) are compared. For lower snowfall rates the agreement between both radar calculations is well, however there are differences at certain time periods: First, MRR calculations resulted in lower snowfall rate values but later with higher snowfall amounts MiRAC showed lower rate values compared to the respectively other instrument values. Thus, an evaluation including synoptical measurements should give more information about the conditions during the event. For this, Figure 6.1 gives an overview about different variables measured during the event relative humidity (RH) [%], temperature [°C], wind speed [m/s], liquid water path (LWP) [g/m²], reflectivity Z_e [dB] averaged between the height of 120 and 180 m, the calculated snowfall rate (S) [mm/h] and by taking the cumulative sum over S, the snow accumulation [mm]. Additionallythe circulation weather type (CWT) is expressed during the whole event. The CWT indicates from which direction the weather is dominant. In this case study the circulation originates from south-west.

The high relative humidity between 84 and 96% at the surface could affect the snow to be rimed. The temperatures at 10 m as well as at 2 m are very similar and well below 0°C around -4 to -4.5°C. The wind speed measurements, also at 2 m and 10 m height, deviate a little more from each other, but just by a maximum of 1 m/s. Over the whole time period of the event they are rather low in between 0.1 m/s to a maximum of 4.6 m/s.

For the LWP a threshold of 500 g/m² is set visually in Figure 6.1, from which present precipitation is assumed to indicate liquid precipitation. As during this case study the temperatures were well below 0°C it could also indicate rimed snow particles or wet snow in the atmosphere. In any case, this threshold is useful to indicate the time at which the MiRAC radome is probably affected by water. The radome which is protecting the radar, became porous over time and lost its hydrophobic coating (personal communication with Alexander Myagkov, RPG). During a long persistent or a short strong precipitation event, the radome absorbs water and the blower is not capable of drying the radome fast enough.

Until 22:00 UTC the LWP stays below this threshold of 500 g/m² but then exceeds

---

[4]click here: `http://gop.meteo.uni-koeln.de/~Hatpro/dataBrowser/dataBrowser1.html?site=Ny-Alesund&date=2018-01-27&UpperLeft=Parsivel_Overview`

it up to a value of 900 g/m^2. Throughout almost the whole day the so called rain flag is set. A rain sensor on HATPRO indicated rain or general precipitation, which could have an affect on the LWP values. Still, the measurements can be a good indicator of qualitatively high or low amount of liquid in the atmosphere.
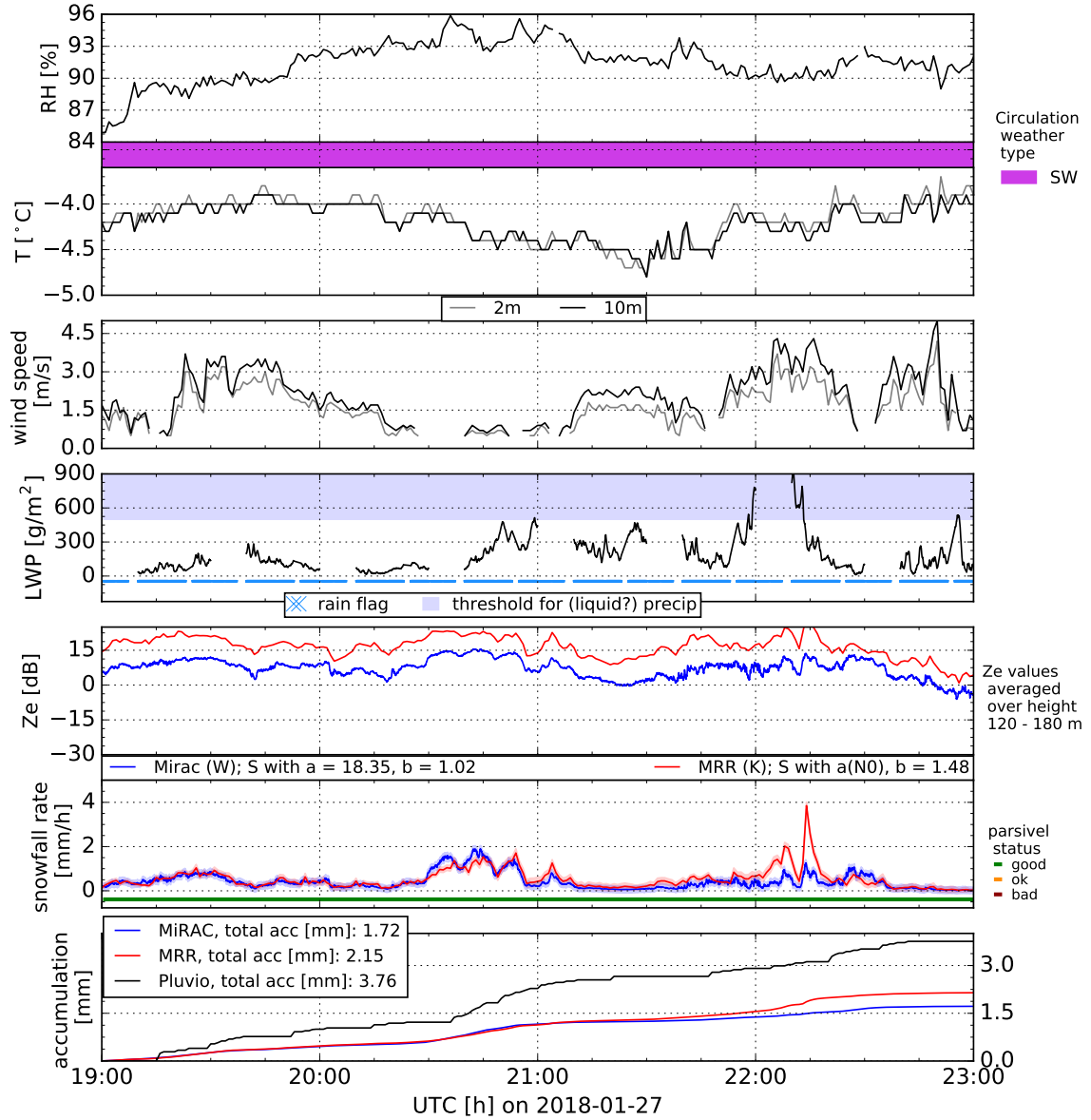
Figure 6.1: Overview of different measured and calculated variables at the site in Ny-Ålesund at January 27th 2018 from 19:00 to 23:00 UTC, from top to bottom panel: relative humidity (RH) (1st panel), circulation weather type color bar (between 1st and 2nd panel), temperature and wind speed at 2 m and 10 m height, respectively (2nd & 3rd panel), liquid water path (LWP) (4th panel), reflectivity and snowfall rate (5th & 6th panel) of MiRAC (blue) and MRR (red), accumulation of snowfall (7th panel) by both radars and for comparison also by Pluvio (black).

Looking at the reflectivities of MRR and MiRAC (Figure 6.1), it can be seen that their difference, also called Dual Wavelength Ratio (DWR), can be up to 10 dB. However, as the radars measure at different frequencies and thus in different scat-

tering regimes, a different reflectivity value range is expected.

Applying the parameters of the snowfall rate retrieval (Table 5.1) to the measured Z_e, the resulting snowfall rates are up to a value of 1 mm/h, but match each other very well. During 20:30 - 20:45 UTC S_{MRR} is smaller than S_{MiRAC}, which cannot be traced back to any of the synoptical measurements. However, for the time period between 21:50 and 22:20 UTC when $S_{MRR} > S_{MiRAC}$ it is speculated that the radome of MiRAC was wet, as generally a high amount of liquid water is present in the atmosphere, regarding the higher LWP values and the rain flag.

The effect of the poorly coated radomes can also be seen in a calibration mismatch when closer looking into the DWR of $Z_{e, MRR}$ minus $Z_{e, MiRAC}$ compared to the reflectivity of MiRAC (Figure 6.2). In lighter grey the same relation is displayed, but from computed reflectivities with simulated radar cross sections from Hyytiälä data (Section 4.2.3). W-Band reflectivities usually have lower values with a maximum of approximately 20 dB, which can be seen in Hyytiälä by the spread of the grey scatter cloud. Comparing the computed scatter values with the measured ones from Ny-Ålesund one sees especially between the range of 0 - 5 dB for $Z_{e, MiRAC}$ higher values for the Ny-Ålesund DWR of about 6 - 7 dB. Additionally, with regard to the calibration error, this could also imply that the derived Z_e-S relationship comprises different snow particle types than observed in Ny-Ålesund.

Figure 6.2: Dual Wavelength Ratio (DWR) of MRR (K-Band) minus MiRAC (W-Band) reflectivities against the MiRAC (W-Band) Z_e. In blue the measured values on 2018-01-27 between 17:00 and 23:00 UTC at the site in Ny-Ålesund and in light grey computed values with data from the measurement site in Hyytiälä.
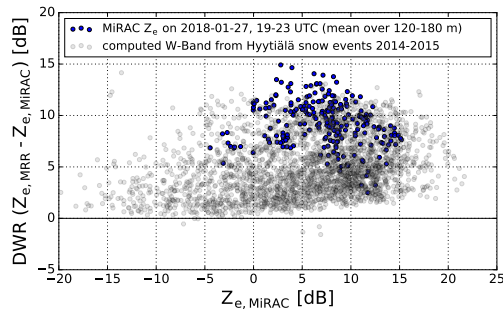
The last panel in Figure 6.1 displays the snow accumulation over the event of both radars and also, for comparison, of the precipitation gauge Pluvio. Due to the light wind conditions an underestimation of Pluvio accumulation values are not expected. Although both radar accumulations fit themselves very well, the total amount of around 1.72 mm to 2.15 mm is much lower than the measured 3.76 mm by Pluvio. Therefore, this first case study shows the ability of the derived Z_e-S relationship to match two different radar reflectivities to a similar snowfall rate. But, as the in situ measurement showed a higher snow accumulation, it might be that the height difference of the radar measurements (mean over 120 to 180 m) and the Pluvio (measured at the surface) is the reason for different values. Precipitation, that the

radar sees aloft can continue to grow during its way through the atmosphere and then more is measured at the surface.

6.1.2   Case study 2: 2018-02-03

On February 3rd the whole day was cloudy (Appendix, Figure A.3). As for the first case study, an overview about different variables are in given in Figure 6.3, which is summarized in the following. Again, as on January 27th, a south-west circulation is the predominant circulation weather type. This case study, however, a more varying relative humidity has been measured throughout the day ranging from 72 to 94%. The temperature has risen continuously from midnight at around -4°C up to -1°C at 14:00 UTC. For the rest of the day, the temperature increased to and above 0°C, which indicates that there could be a mixture of snow and rain. Thus, the event to be analyzed is restricted until 14:00 UTC to account for solid precipitation only. No difference can be seen between the 2 m and 10 m temperature measurements. The wind speed varies from 6 m/s up to 9 m/s and down to 1 m/s during the night until 07:00 UTC. During the day the variation is again high, from 6 m/s up to 12 m/s until 14:00 UTC. These high alternating wind speeds affect Pluvio measurements. LWP values also vary a lot between 20 g/m^2 up to just above 500 g/m^2. The reflectivity difference between both radars is not as large as in the first case study, but $Z_{e,MRR}$ often drops down to its sensitivity values of -14 dB. Despite these inhomogeneous conditions the two radar snowfall rates match very well. Also, the higher peaks at 12:00, and 14:00 UTC are registered by both, albeit not in the exact intensity; MiRAC shows slightly higher values for the snowfall rate than MRR. However, during a 20-minute snow event from 9:00 UTC on, MRR has a higher snowfall rates. Comparing the accumulation of the snowfall rate with Pluvio measurements, Pluvio shows 1.3 - 2 mm lower accumulation values compared to the previous case study. Due to the high winds during the day, this is not surprising, as a lot of snow could be blown over the Pluvio orifice and thus, not be captured. The undercatchment of solid precipitation at moderate to high wind speeds is one of the main disadvantages of gauge measurements and a lot of research has been done in this field. Based on SPICE, correction functions have been empirically determined to correct gauge measurements (Section 4.1.3). Recently developed functions by K17 (Eq. (11)) and W15 have been applied to uncorrected Pluvio accumulation measurements at Ny-Ålesund (Figure 6.4).

For applying the correction functions, wind speed and temperature are averaged at a height of 2 m (gauge height) over 30 minutes and the accumulated sum of the prevailing precipitation over the same 30 minutes are used. The progression of the
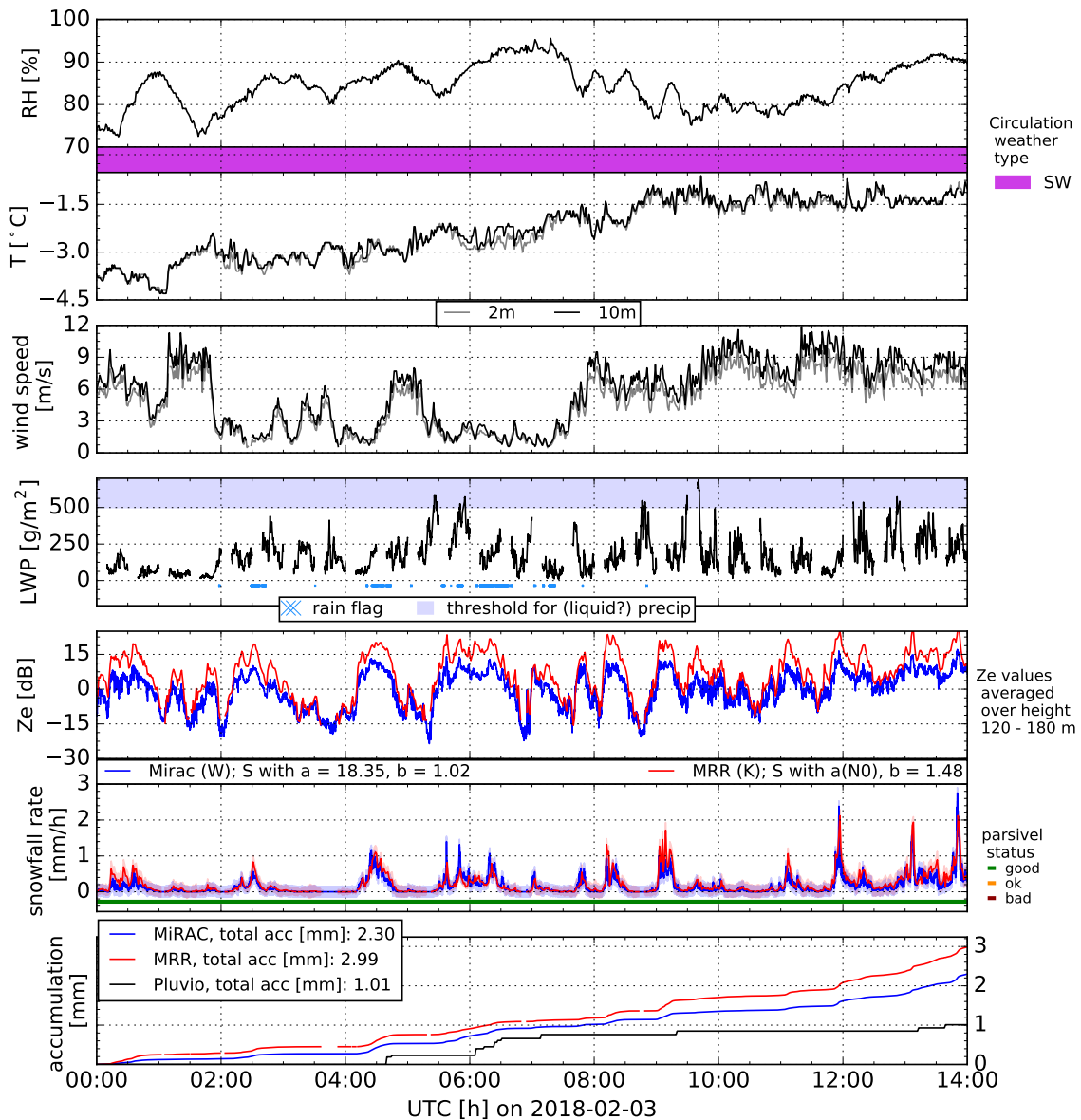
Figure 6.3: As in Figure 6.1 but for February 3rd 2018.

three different accumulated precipitation values of Pluvio, the correction applied by K17 and the one by W15 are shown in the top panel of Figure 6.4. At the end of the event (14:00 UTC) the difference between the uncorrected values and the corrected, but also among the two corrected values themselves, is significant. With the correction by K17 the total amount is calculated to 1.41 mm which is about 0.4 mm more than was obtained from the uncorrected measurement. The correction by W15 has a value of even 0.55 mm higher. This spread within the correction factors in itself shows that it is not trivial to grasp the right amount of precipitation. Compared to the calculated accumulation from the radars, the corrected gauge values are still lower by 0.34 - 0.9 mm (MiRAC) and 1.02 - 1.6 mm (MRR).

This case study nicely shows the drawback of surface in situ and radar measure-
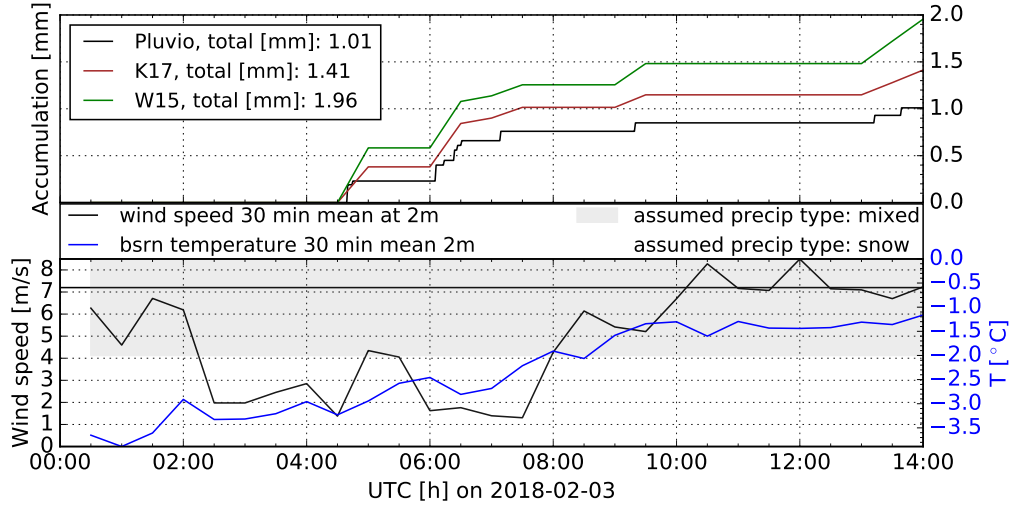
Figure 6.4: Top: accumulated precipitation of uncorrected Pluvio data (black) and 2 differently corrected accumulations by *Kochendorfer* et al. (2017, hereafter K17) (brown) and *Wolff* et al. (2015) (green), both depending on temperature and wind. Bottom: wind speed (black) and temperature (blue) at a height of 2 m averaged to half hour ranges. A solid black line indicates the threshold of 7.2 m/s used in the correction functions of K17. For temperatures between +2°C and -2°C, the assumed precipitation type is mixed, thus it can be rain and snow. Below -2°C snow is assumed. Different parameter values have to be used in the correction functions depending on the precipitation type.

ments. But, not only the wind and temperature play a role for the discrepancy in the accumulation, but also the height difference at which the instruments measure. In contrast to case study 1, the Pluvio in this case study indicates to have less precipitation at the surface than what the radars measure aloft. It thus could also be the case, that the precipitation evaporates before it reaches the surface.

Similar to the previous section, the scatter plot in Figure 6.5 shows the measured DWR against $Z_{e,\ MiRAC}$ but this time also for MRR. The computed reflectivity from Hyytiälä data is the grey scatterplot. For this case study, on February 3rd, the Ny-Ålesund reflectivity differences agree with the Hyytiälä scatter plot. They match each other which is consistent with the matching snowfall rates. This DWR plot in comparison to the previous (Figure 6.2) implies that on this day the observed snow type in Ny-Ålesund fits the types from the Hyytiälä dataset better.

6.1.3   Case study 3: 2018-03-14

During the night from March 13th to March 14th clouds formed and right after midnight precipitation started (Appendix, Figure A.4). Low temperatures between -7°C and -8.4°C, low wind speeds up to a maximum of 4.5 m/s until 14:00 UTC and very low LWP in the atmosphere around the sensitivity of the instrument with 20 g/m²
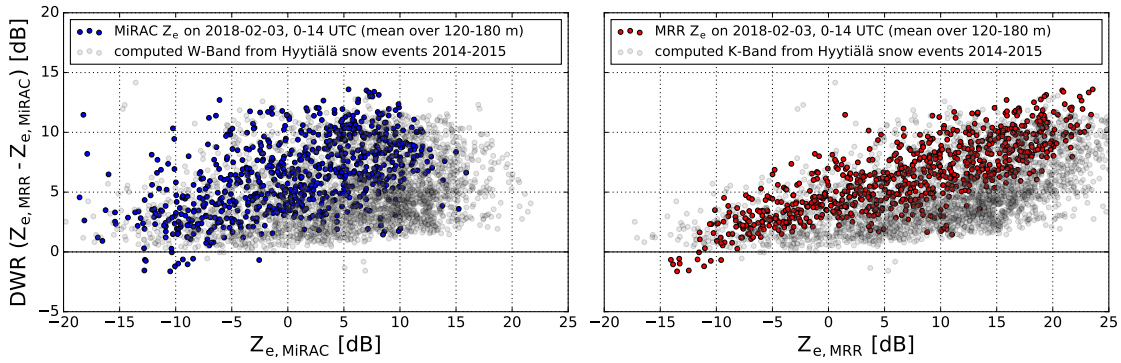
Figure 6.5: Left: As in Figure 6.2 but for measured values on 2018-02-03 between 00:00 and 23:00 UTC. Right: Similar to left, but DWR against MRR (K-Band) Z_e in red.

(Appendix, Figure A.5) could indicate unrimed snow particles and are perfect conditions for the retrieval application of the Z_e-S relationship. Yet, comparing the reflectivity values, a problem directly becomes evident: $Z_{e, MRR}$ has values as low as -10 dB and not only that, but also lower than $Z_{e, MiRAC}$ values (Figure 6.6, top panel). This propagates into the snowfall rate which results in a mismatch (Figure 6.6, bottom panel). Although at first, both snowfall rates seem to match (00:00 - 00:20 UTC), a distinct drop in $Z_{e, MRR}$ causes S_{MRR} to drop as well. After one hour, at 01:20 UTC MRR reflectivity values seem to recover, which is also evident in S_{MRR}. Shortly afterwards another drop happens and the same progression occurs again at 03:45 UTC and 09:45 UTC.
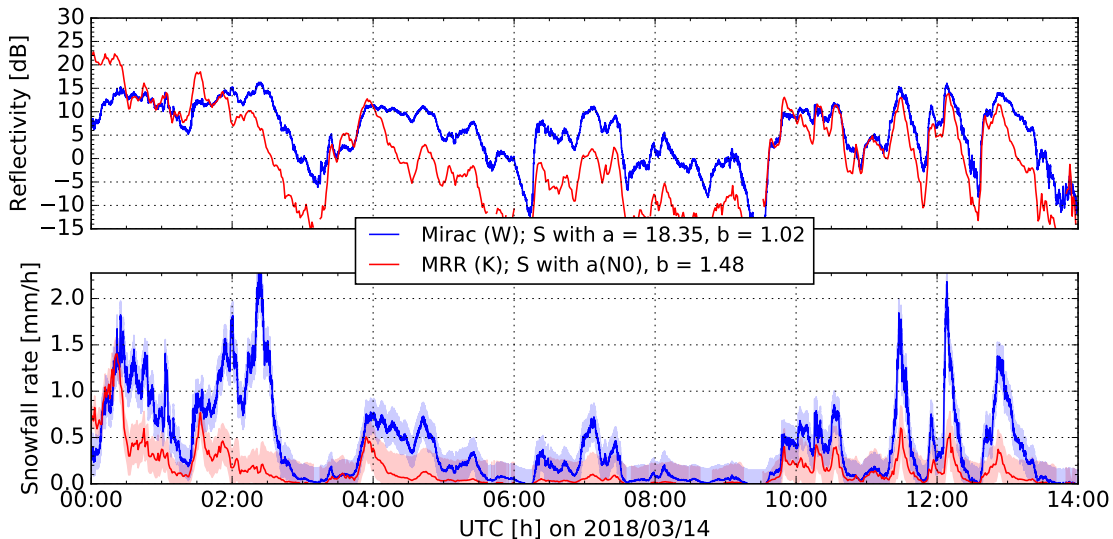
Figure 6.6: Top: Reflectivity values of MiRAC (blue) and MRR (red) on March 14th 2018. Bottom: Calculated snowfall rate values for the same instruments and time.

The hypothesis for $Z_{e, MRR} < Z_{e, MiRAC}$ is attenuation due to something very close to or on the antenna dish of MRR. This could happen, for example, when a lot of snow accumulates on the dish, which might have happened in this case study.

As $Z_{e,MiRAC}$ shows a high snowfall rate above 1.5 mm/h and Pluvio has a high accumulation during the whole day (Appendix, bottom panel of Figure A.5), even higher than MiRAC, this case study is a strong snow event. The built-in heater usually prevents accumulation by melting the snow which can then drain easily from the tilted antenna dish. If the precipitation event is too strong, then the heater is not fast enough and half melted (wet) snow remains too long on the dish, might even freeze and affects scattering processes. *Maahn and Kollias* (2012) have found similar heating problems with K-Band radars, especially for wet snow events. The radar signal, which is usually redirected vertically into the atmosphere by the antenna dish, gets scattered by water or ice particles on the dish isotropically leading to a reduced backscattered signal to the receiver. For the sake of completeness and to better understand which quantitative difference between $Z_{e, MRR}$ and $Z_{e, MiRAC}$ values are to be expected, Figure 6.7 shows the DWR of simulated K-Band and W-Band reflectivities ($Z_{e,K}$ and $Z_{e,W}$) as 2D density plot with frequency distributions along each dimension. The reflectivity values are simulated from the Hyytiälä dataset of two winters in 2014 and 2015 and for snow events only. It can easily be seen how large the DWR can become at a certain $Z_{e,K}$ or $Z_{e,W}$, respectively. For example at a $Z_{e,W}$ value of 10 dB it is most likely to have a $Z_{e,K}$ that should be at least 3 dB higher. Thus, the measurements of the reflectivity in this case study 3 are simply physically not correct. Nevertheless, this result showed - without previously knowing - that the heater of the MRR was running and could now be turned off to prevent a recurrence.
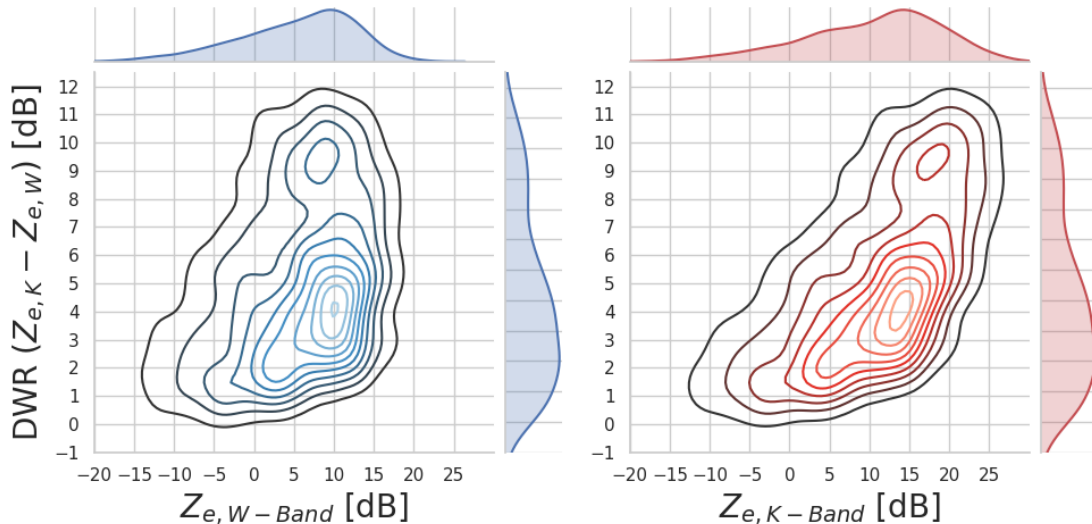
Figure 6.7: 2D density plot of Dual Wavelength Ratio (DWR) of simulated K-Band minus simulated W-Band reflectivities against W-Band and K-Band Z_e, in blue and red, respectively. For each axis a frequency distribution is displayed.

6.1.4 Case study 4: 2018-03-15

In the morning of March 15th 2018 high clouds developed and descended until they reached the ground at noon (Appendix, Figure A.6). Only during the afternoon at around 17:00 UTC PARSIVEL recorded particles and classified them as snow (see Quicklook Browser[5]). Reflectivity values detected by MiRAC of up to 15 dB, close to the surface, also indicated precipitation. The RH at the surface was drier than in the previous case studies with a minimum of 72% and not exceeding 81% until 20:00 UTC. The overall maximum during the whole day was 86%. LWP was above 100 g/m^2 only for a short time span with a maximum of 250 g/m^2 at 19:30 UTC, but otherwise staying below 100 g/m^2. Temperatures were around -7°C and wind speeds were high with 8 - 12 m/s until 21:00 UTC and then reduced down to 4 m/s. These synoptic overview measurements can be seen in the Appendix in Figure A.7 and present fairly good weather conditions for snowfall measurements. Yet, for Pluvio the wind speed is too high and an undercatchment can be assumed (Appendix, bottom panel of Figure A.7). Looking at the different reflectivity values in the top
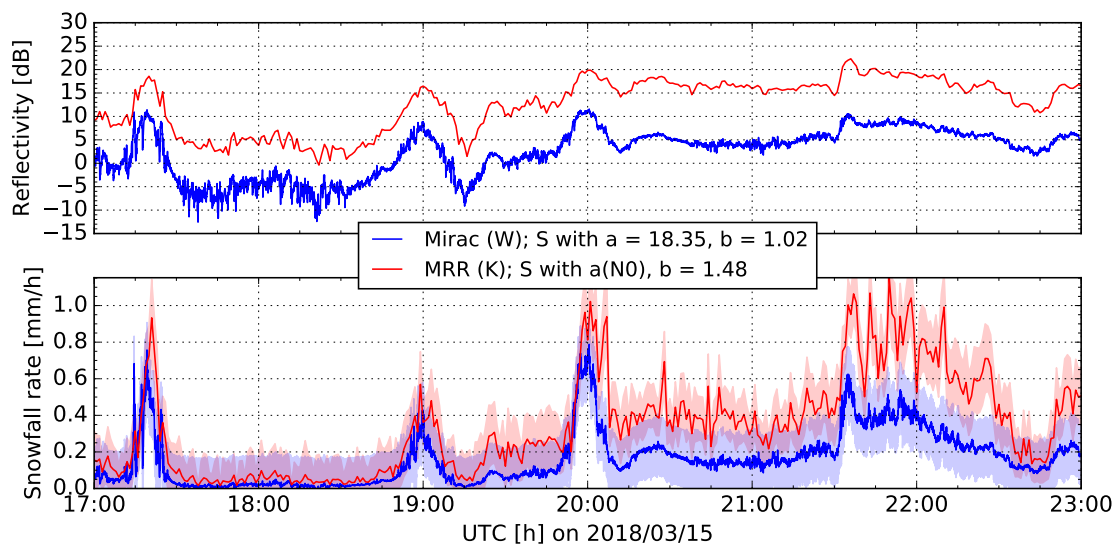
Figure 6.8: As in Figure 6.6 but for March 15th 2018.

panel of Figure 6.8, their difference is quite large with values between 8 - 14 dBZ. The resulting snowfall rate only matches the smaller values until 19:00 UTC but then S_{MRR} starts deviating from S_{MiRAC} in the same time when the reflectivity difference is large. As one cannot draw any obvious conclusions from the previous mentioned synoptical observations about the mismatch in snowfall rate, a closer look into the DWR could give an answer. The displayed DWR in Figure 6.9 against $Z_{e,MiRAC}$ and

---
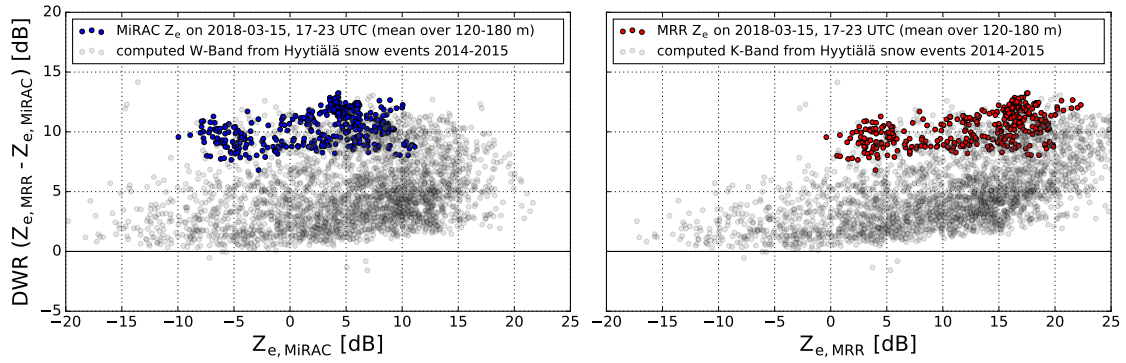
Figure 6.9: As in Figure 6.5 but for March 15th 2018.

$Z_{e,MRR}$ directly shows that there is an offset on this day. Whereas for the other case studies most of the reflectivity values matched the calculated ones, in this case at least a difference of 8 dBZ is visible. Again, just more pronounced than in Figure 6.2, either the calibration at one or both of the instruments was wrong or the hypothesis can be proposed that a different snow type is more dominant in Hyytiälä than in Ny-Ålesund or vice-versa. Thus, the developed Z_e-S relationship might not be suitable for this snow event.

6.1.5   Case study 5: 2018-03-16

March 16th 2018 was an overcast day. Low clouds were present the whole time with almost continuous high reflectivity values throughout the day indicating stratiform precipitation (Appendix, Figure A.8). The DWR of both radars are comparable to the calculated Hyytiälä DWR values (Appendix, Figure A.10). The temperatures were well below 0°C until noon with around -6°C, rising up until -3°C towards the end of the day (Appendix, Figure A.9). Low wind speeds of around 3 m/s from 03:00 UTC on, as well as low LWP values around 100 g/m^2 were good conditions to apply the Z_e-S relationship parameters to the snowfall measured radar reflectivities and compare the cumulative sum of the calculated snowfall rates with gauge accumulation measurements (Figure 6.10). The snowfall rate values from both radars match during the whole day very well. Only for a higher peak at 02:00 UTC and between 20:00 - 21:00 UTC the snowfall rate calculated from $Z_{e,MRR}$ has higher values than the snowfall rate results from $Z_{e,MiRAC}$. However, the values lie within the uncertainty range.

At a stronger snowfall rate event at around 02:00 UTC the wind speeds dropped from 9 m/s to 6 m/s, still high enough for the Pluvio to underestimate the actual snow amount. This could be the reason for a delay of half an hour in the onset of Pluvio's accumulation at 2:30 UTC. Thus, the two correction functions by K17 and

W15 (Section 6.1.1) were applied to the uncorrected Pluvio data (Figure 6.11) to account for a possible wind undercatch. Due to the usage of a 30 minute mean for temperature and wind speed the higher winds at the strong event at 2:00 UTC are averaged out. Still, both corrections indicate in total about 0.4 (K17) and 0.55 mm (W15) more precipitation than the uncorrected. Comparing these corrected values to the total calculated accumulations by the radars, the difference to the MiRAC values is only 0.47 (K17) and 0.29 mm (W15) whereas to the MRR values it is around 1 mm.

Despite the, in general, well matching snowfall rate of the radars the cumulative sum of both snowfall rates show that the Z_e-S relationship for the MRR accumulation values were 0.6 mm higher than MiRAC's, which are the consequence of few higher S_{MRR} values.
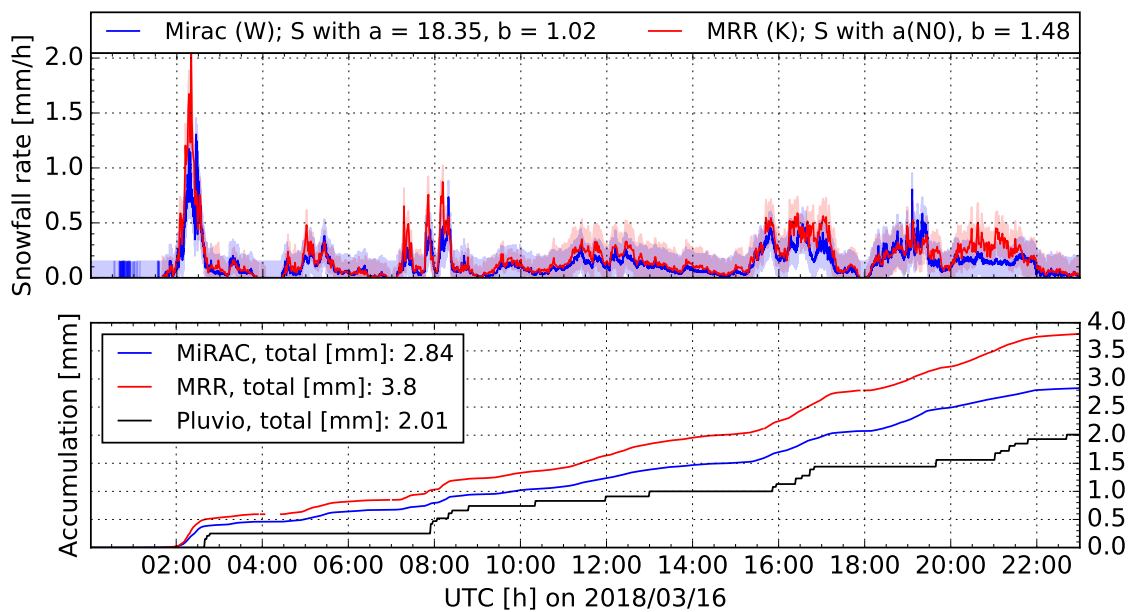
Figure 6.10: Top: Calculated snowfall rate values of MiRAC (blue) and MRR (red) for March 16th 2018. Bottom: Accumulation of the calculated snowfall from the radars and of the gauge measurements (black).
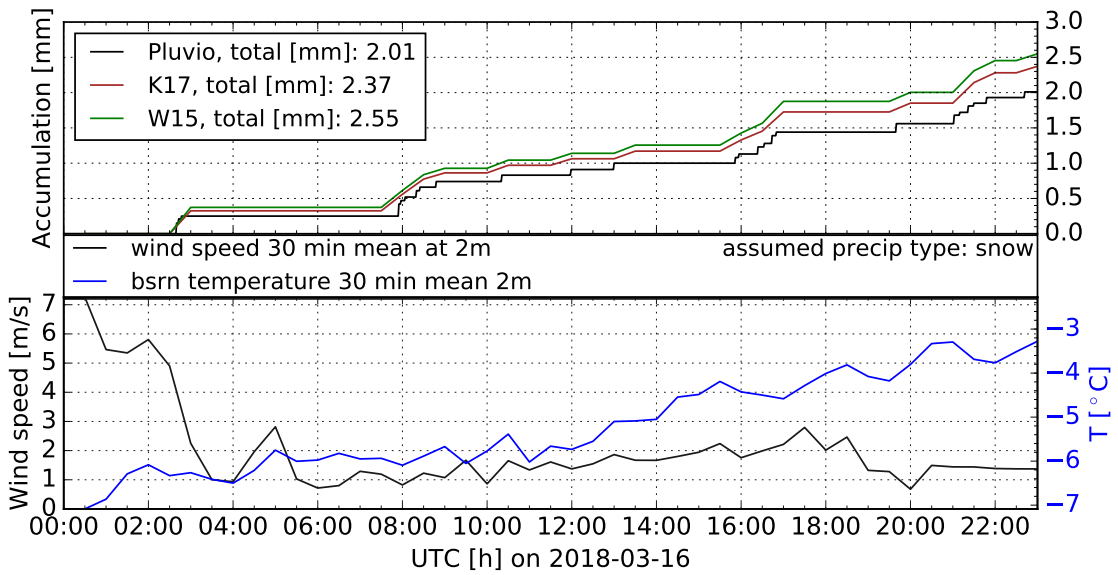
Figure 6.11: As in Figure 6.4 but for March 16th 2018.

6.2   Uncertainty discussion

In total, the obtained results are satisfying but also reveal challenges in the retrieval of snowfall rate with the Z_e-S relationship and that different uncertainty factors do exist. In general, the comparison of surface observations with remote sensing measured and derived variables is difficult for itself: A measurement at one point at the ground compared with a volume of observed particles in a few hundred meters height leads to an unknown uncertainty factor. Several interactions of particles and other microphysical processes can happen within this height difference. Furthermore the instruments themselves have uncertainties. Radar measurement uncertainties are due to the sensitivity of reflectivity, attenuation and calibration. The uncertainties of disdrometers are dependent on the measurement principle (video, laser) and the derived variables e.g. fall velocity, PSD and especially the measured dimension of the particle. Pluvio has uncertainties during high wind and blowing snow conditions, which can partly be compensated for with correction functions, but the two applied functions showed different amounts among one another, revealing the true precipitation amount to be somewhere in between both.

Souverijns et al. (2017) used a MRR and PIP to retrieve their own Z_e-S relationship over Antarctica and quantitatively estimated uncertainties for three different categories: measurement, shape and parameter. They investigated on the contribution of each variable in Eq. (9) and (13) for S and Z_e, respectively, to each uncertainty category. According to their findings, the uncertainty in the derivation of the mass of snowflakes has the highest uncertainty influence to the Z_e-S relationship, together

with the variability of microphysical processes and snowflake characteristics during observed snow storms. The evaluation of *Souverijns* et al. (2017) was done for dry snowfall only and riming has not been considered. However, Ny-Ålesund is located at a coast (where riming processes do take place) and also Hyytiälä has a reasonable amount of rimed snow particles (*Moisseev* et al., 2017). Despite that, the qualitative results from *Souverijns* et al. (2017) are transferable to the findings in this thesis: the consistency of the snowfall rate between a K- and W-Band radar is dependent on 1. the snowfall event and 2. the different snowflake shape, density or mass which might have occurred and measured at Hyytiälä differently than at Ny-Ålesund. Furthermore, PSD can have a large influence on the snowfall rate retrieval. Especially in the snowfall rate retrieval in this work, the prefactor a_{zs} is set in dependency of the intercept parameter N_0 of the PSD. Thus, the uncertainty from PSD measurements of PARSIVEL, which is connected to the measurement of the snowflake dimension (Section 4.1.2 and *Battaglia* et al., 2010), propagates into the uncertainty of the derived snowfall rate.

7   Summary and outlook

The aim of this thesis was twofold: the derivation of a new snowfall rate retrieval for two radar frequencies at one measurement site at a high latitude and its application as well as its evaluation at another measurement site in the Arctic. Radar-based snowfall rate retrievals are derived from the relationship between the equivalent reflectivity Z_e and snowfall rate S. Traditionally, this is a power law relationship. The prefactor a_{zs} and exponent b_{zs} are the parameters to be derived as a first step.

At the measurement station in Ny-Ålesund, Svalbard only within the last 2-3 years a laser-disdrometer, a K-Band (24 GHz) radar and a W-Band (94 GHz) cloud radar have been installed. A synergy of continuous remote sensing measurements could thus not be provided until recently. Therefore, an own Z_e-S relationship for these two newly installed radar frequencies has not yet been available for Ny-Ålesund, literature relationships have been used so far.

However, a dataset of snowfall events observed during the two consecutive winters of 2014/2015 (*Moisseev*, 2018) at the measurement site in Hyytiälä, Finland is available. At this site, a video-disdrometer is operated, which is better suited for snowfall observations than a laser-disdrometer, due to a more accurate derivation of snow properties.

For this thesis the snowfall rate was calculated from the Hyytiälä dataset and together with two forward models (TMM and DDA) the radar cross section was simulated to calculate radar reflectivity. A relationship between Z_e and S was then empirically derived via two methods: Method 1 comprises the fit parameters of a total least squares fit of 3012 available 5-minute measurements and simulations, called the average Z_e-S relationship parameters. Method 2 is an analytical approach which evaluates for each time step the dependency of the prefactor a_{zs} and exponent b_{zs} to each variable that describes Z_e and S. The main contributor to the prefactor is the intercept parameter N_0 (*Rasmussen* et al., 2003; *von Lerber* et al., 2017) of the assumed exponential snow particle size distribution. Thus within this thesis, a_{zs} was used in dependency of $N_0(t)$ and from the time dependent b_{zs} values a mean value was calculated and used. An uncertainty assessment revealed that the analytical Z_e-S relationship for K-Band significantly reduces the uncertainty in S when compared to the average relationship. For W-Band the uncertainty of the average relationship is slightly lower than the analytical. Thus, method 2 ($a(N_0(t))$ and b= 1.48) is used for K-Band and method 1 (a= 18.35 and b= 1.02) for W-Band.

To obtain radar-based snowfall rate information at the station in Ny-Ålesund, these new Z_e-S relationship parameters were applied to the measured radar reflectivities of the K-Band and the W-Band radar. Five case studies from January to March

2018 were evaluated in more detail. For a comparison to the weighing precipitation gauge Pluvio, the snowfall rates were accumulated. To get a better overview of the atmospheric conditions during the snow events, temperature, relative humidity, wind speed, LWP, the circulation weather type and the reflectivity were used as auxiliary measurements and also investigated. At days with high wind speeds, the Pluvio is likely to suffer from wind undercatch and thus two correction functions were applied to the snow accumulation of the uncorrected Pluvio measurements.

In general, it can be concluded that two out of these five days (case study 2 and 5) show very well matching snowfall rates when only looking at the radar-based snowfall rates. Compared to Pluvio accumulations and applied corrections, the difference of the two snow accumulations from the radars can range between 0.34 - 2 mm on February 2nd and between 0.29 - 1.17 mm on March 16th. For case study 1 and 4 the snowfall rate of both radars matches most of the time. However, a DWR offset of 6-8 dBZ advances two hypotheses: Either one or both radars are miss-calibrated or the snow particle types are different in Hyytiälä and in Ny-Ålesund. Different snow particles habits result in different radar reflectivity values and hence adapted snowfall rate retrieval parameters would be needed to use. Case study 3 reveals the drawback of the MRR heating system for strong snow events: the dish heater was not able to melt the accumulated snow on the dish fast enough, which resulted in a significant attenuation of the signal at the receiver. Despite that, the accumulated snowfall rate calculated from $Z_{e, MiRAC}$ for case study 3 shows a difference of ca. 2 mm to the total amount of the uncorrected Pluvio data.

Different sources of uncertainty are discussed qualitatively which include the various instrumentation uncertainties, the comparison of point to volume measurements and the uncertainty of the diverse snow habits present in Hyytiälä and in Ny-Ålesund. All in all, taking into account the numerous error sources that start off from the snowfall rate retrieval itself and propagate from the previously mentioned uncertainties into the final result, the aim of deriving snowfall rates at Ny-Ålesund from two radars is satisfactorily achieved.

For future studies, a longer measurement time series could cover a wider range of different snow habits and then be investigated in more detail. A more thorough study of what kind of snow particle growth takes place or even dominates at Ny-Ålesund (aggregation or riming) could, however, be better possible with a triple frequency approach (e.g. *Kneifel* et al., 2011a, 2015). This would mean adding a third radar to the measurement site. Furthermore, reliable particle mass measurements at Ny-Ålesund are important, due to the conclusion of *Souverijns* et al. (2017) that estimates of the snowflake mass must be significantly improved to re-

duce uncertainties due to the shape or size of the particle. The mass of a snowflake is required if an individual Z_e-S relationship for the station at Ny-Ålesund itself is to be retrieved. This gap could be bridged by installing a video-disdrometer or an instrument with the same, similar, or improved capabilities to measure falling snow particles.

Nevertheless, with the current available instrumentation set-up, it would be possible to continue the work of this thesis by implementing the applied Z_e-S relationships into an operational use. However, an algorithm would need to distinguish between solid and liquid precipitation, which could be used from PARSIVEL's hydrometeor classification product. The latter distinguishes between eight different precipitation types.

To get a general overview of all available snowfall rate values, the derived results from this thesis could be compared with CloudSat's CPR observations (or other future satellite missions such as EarthCare) and the ERA5 snowfall rate. A continuous time series of snowfall measurements/calculations could for example validate the obtained snowfall accumulation in Figure 1.1.

A further investigation on the wind effects and especially the orographic influence of the mountains and the Fjord (*Maturilli* et al., 2013) would also be necessary and helpful to understand the occurrence of snow events and their linkage to the calculated snowfall rate discrepancies. Wind cube measurements for example could provide a better overview of snowfall movement within the atmosphere and thus an improved comparison of radar and surface measurements.

A   Appendix

Table A.1: For MRR: Value range of prefactor a_{zs} in Z_e-S relationship and range, and mean of RMSE values for snowfall rate S_{MRR}.

case study	min a_{zs}	max a_{zs}	RMSE of S [mm/h]	mean RMSE
2018-01-27, 19-23 UTC	65.10	720.53	0.027 to 0.208	0.131
2018-02-03, 00-14 UTC	35.17	1154.38	0.002 to 0.254	0.135
2018-03-14, 00-14 UTC	30.41	745.62	0.025 to 0.265	0.196
2018-03-15, 17-23 UTC	63.08	1130.89	0.006 to 0.210	0.137
2018-03-16, 00-23 UTC	50.29	1436.14	0.001 to 0.227	0.126
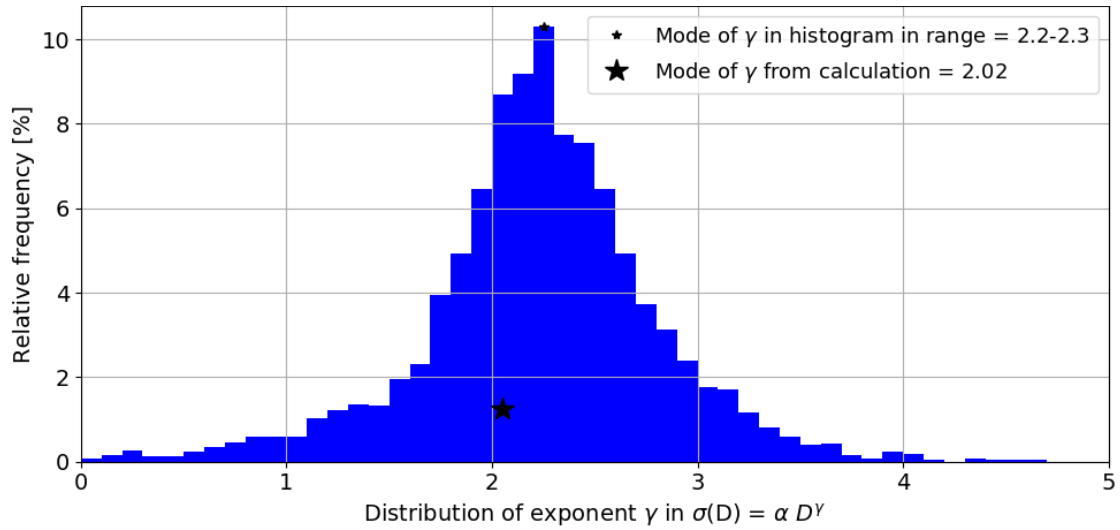
Figure A.1: The distribution of the exponent γ from the power-law $\sigma(D) = \alpha \, D^{\gamma}$. Variable D is the snow particle dimension. The backscatter cross section ($\sigma(D)$) is simulated with the T-Matrix Method for the wavelength $\lambda = 3.19$ mm. For the latter mass and snow particle diameter are used from a dataset of 5-minute snow measurements for two consecutive winters 2014/2015. The distribution values result from a polynomial fit from which the calculated mode value with two decimal places is calculated and displayed with a large black star. The histogram bin range is 0.1 and the histogram mode value is shown with a small black star.
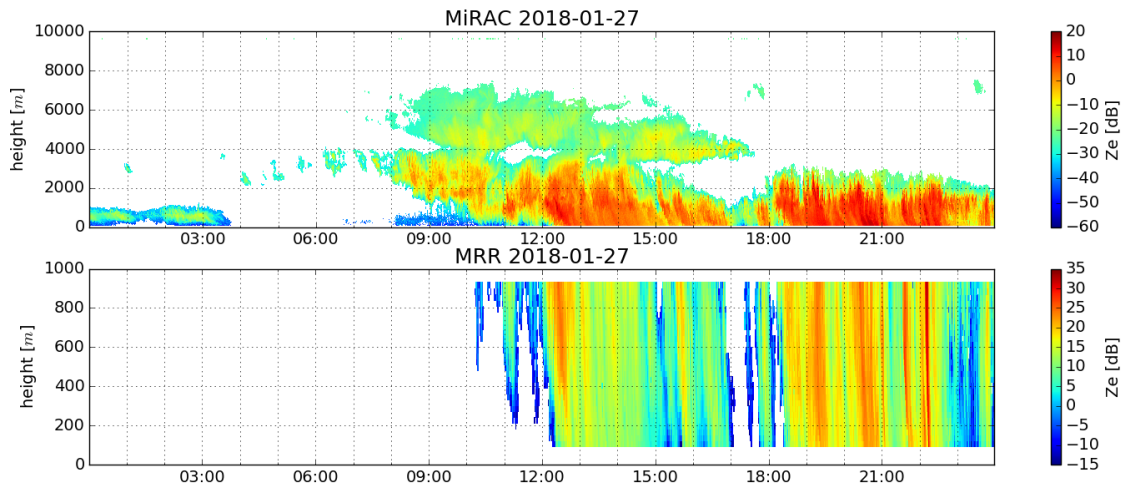
Figure A.2: Time-height plot of equivalent reflectivity values on January 27th 2018 for MiRAC (top) and MRR (top). Note the different y-axis and colorbar ranges.
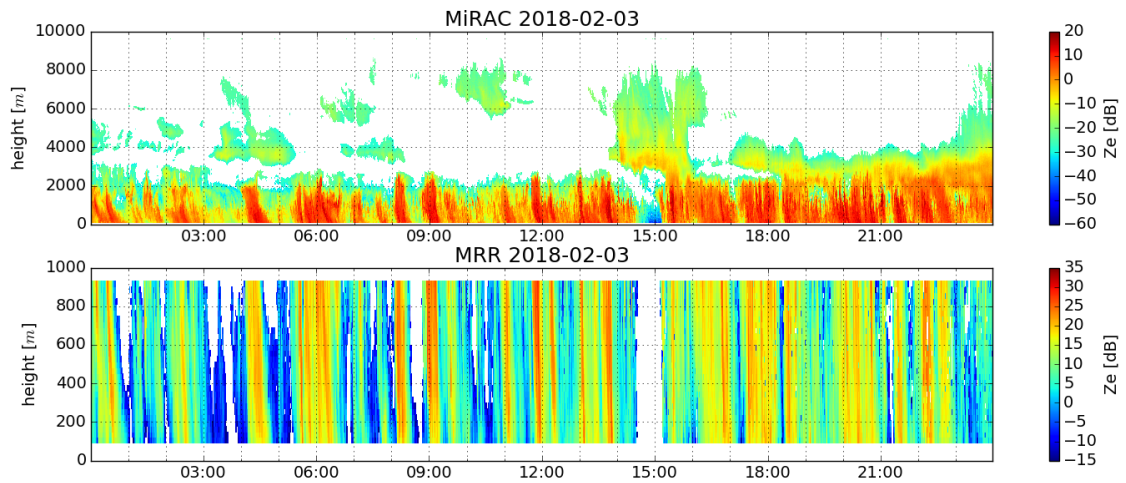
Figure A.3: Time-height plot of equivalent reflectivity values on February 3rd 2018 for MiRAC (top) and MRR (top). Note the different y-axis and colorbar ranges.
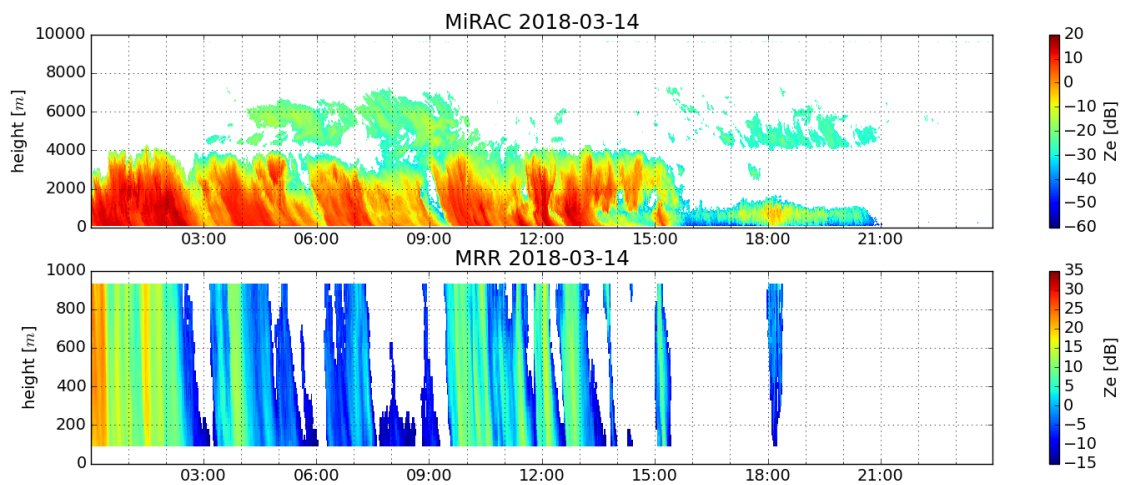
Figure A.4: Time-height plot of equivalent reflectivity values on March 14th 2018 for MiRAC (top) and MRR (top). Note the different y-axis and colorbar ranges.
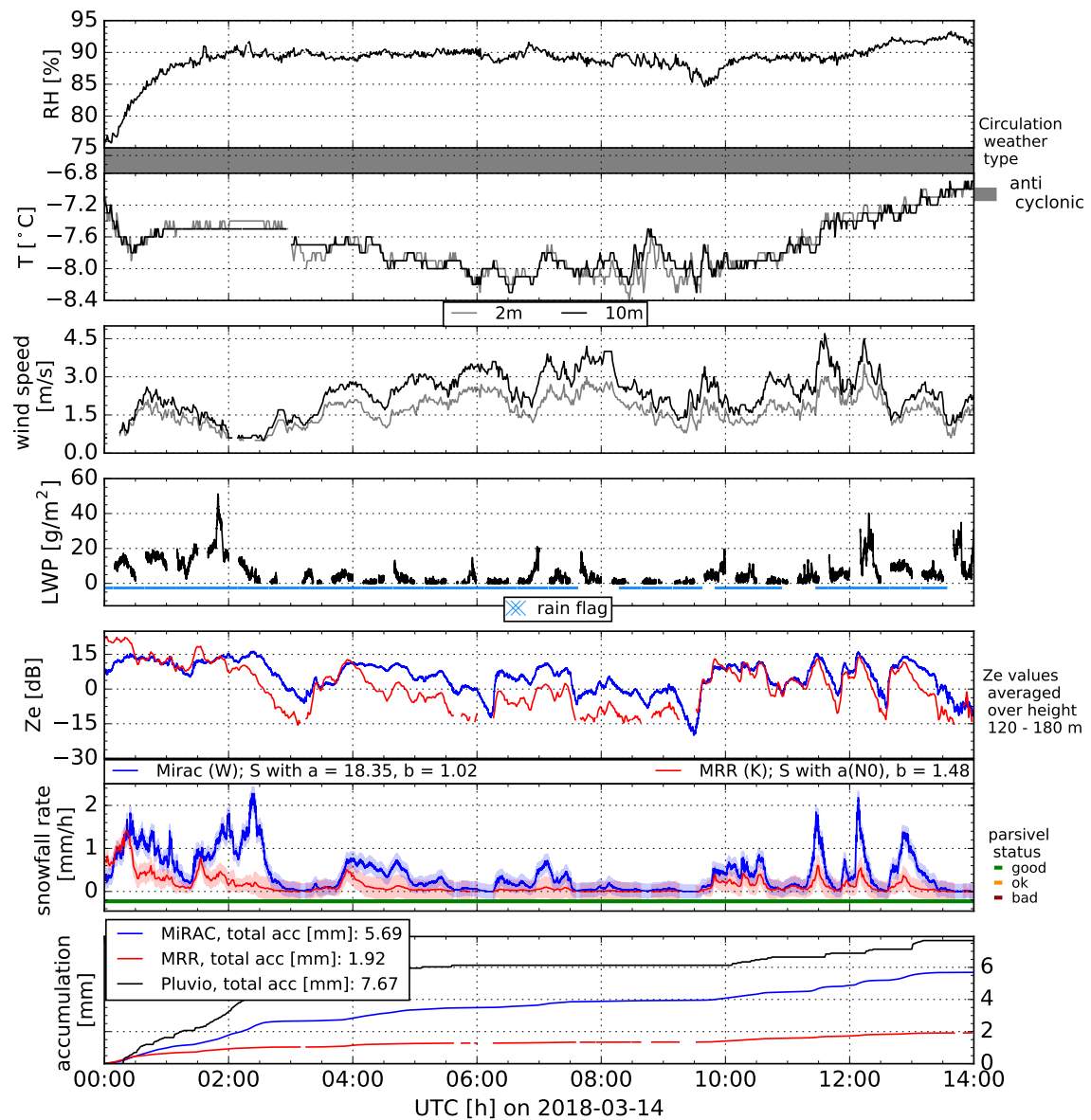
Figure A.5: Overview of different measured and calculated variables at the site in Ny-Ålesund on March 14th 2018, 00:00 to 14:00 UTC, from top to bottom panel: relative humidity (RH) (1st panel), circulation weather type color bar (between 1st and 2nd panel), temperature and wind speed at 2 and 10 m height, respectively (2nd & 3rd panel), liquid water path (LWP) (4th panel), reflectivity and snowfall rate (5th & 6th panel) of MiRAC (blue) and MRR (red), accumulation of snowfall (7th panel) by both radars and for comparison also by Pluvio (black).
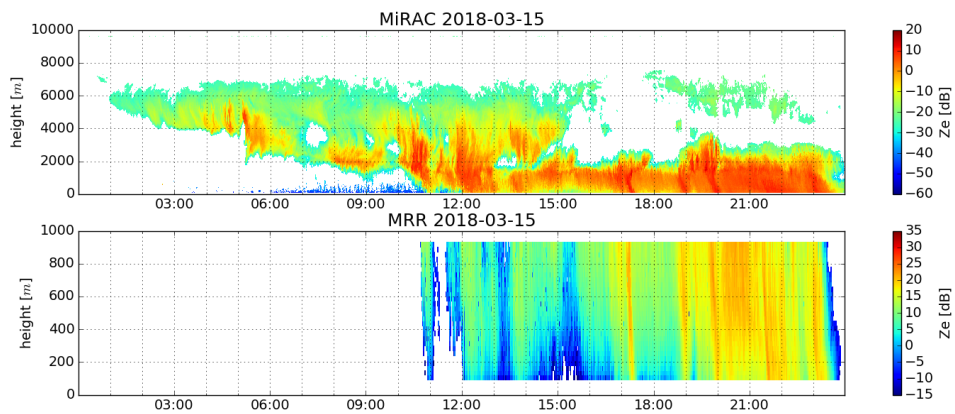
Figure A.6: Time-height plot of equivalent reflectivity values on March 15th 2018 for MiRAC (top) and MRR (top). Note the different y-axis and colorbar ranges.
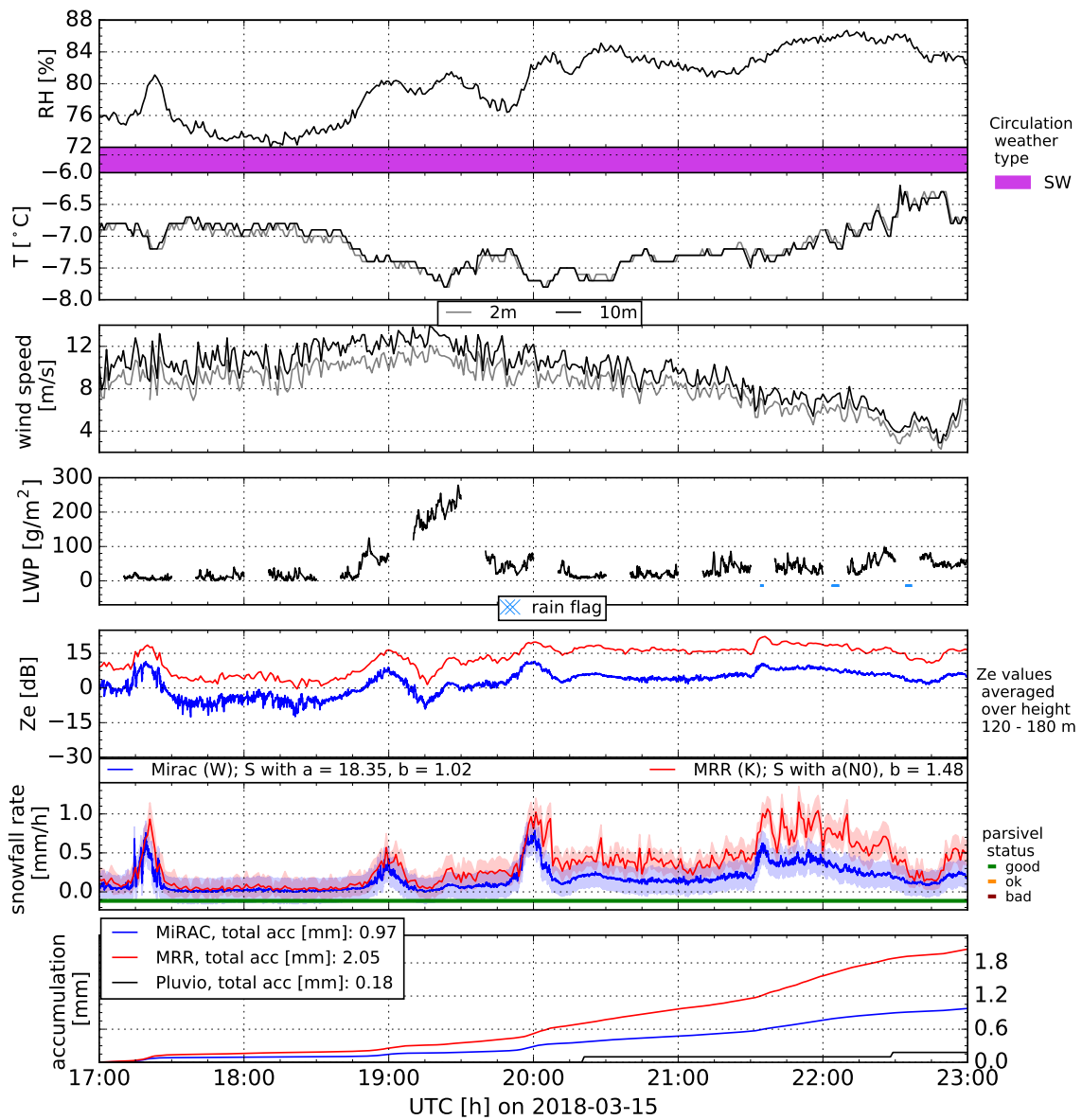
Figure A.7: As in Figure A.5 but for March 15th 2018.
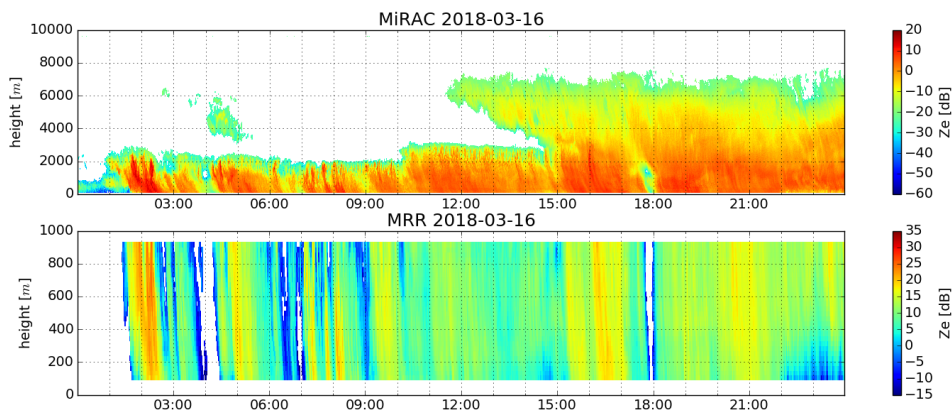
Figure A.8: Time-height plot of equivalent reflectivity values on March 16th 2018 for MiRAC (top) and MRR (top). Note the different y-axis and colorbar ranges.
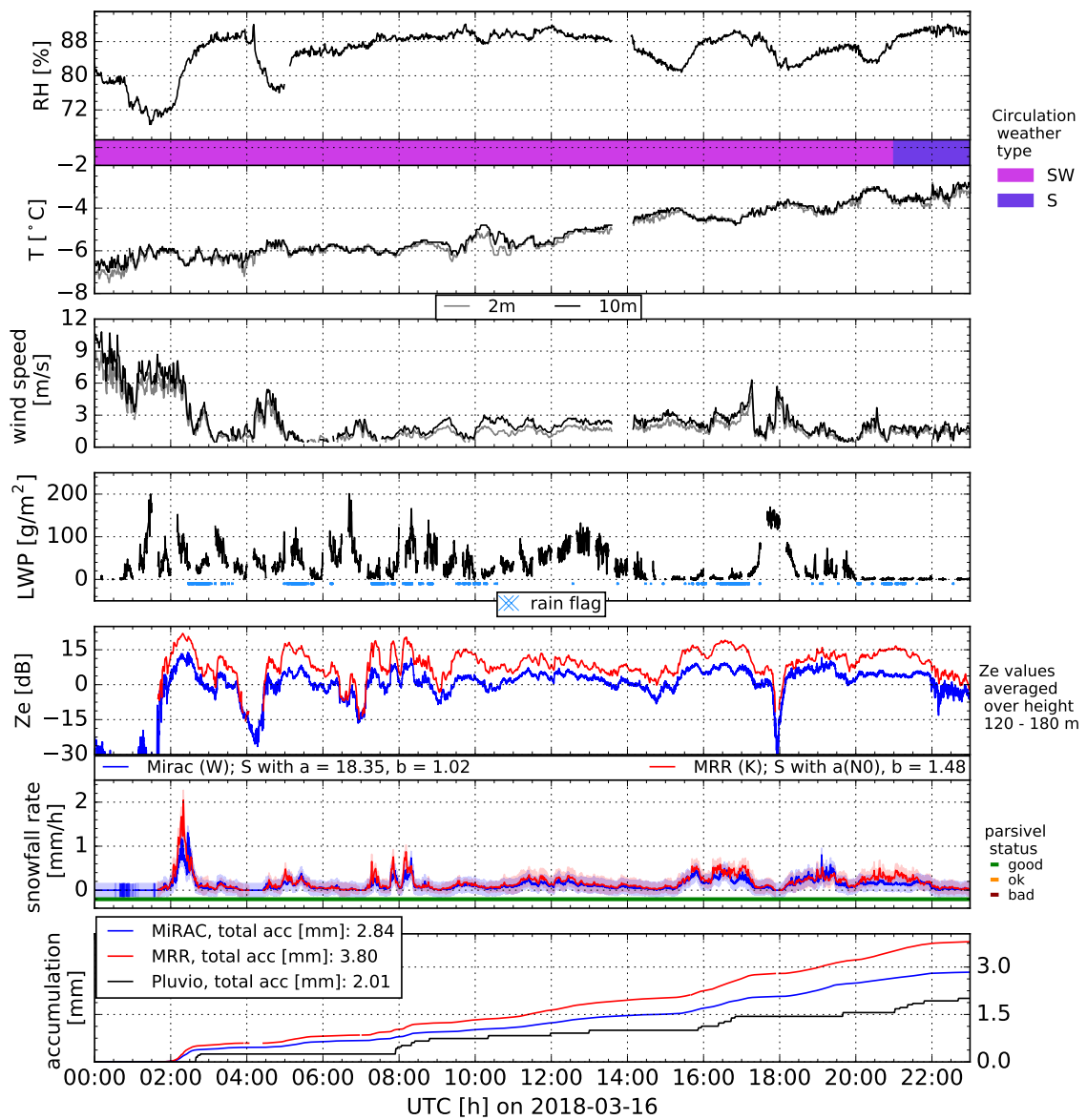
Figure A.9: As in Figure A.5 but for March 16th 2018.
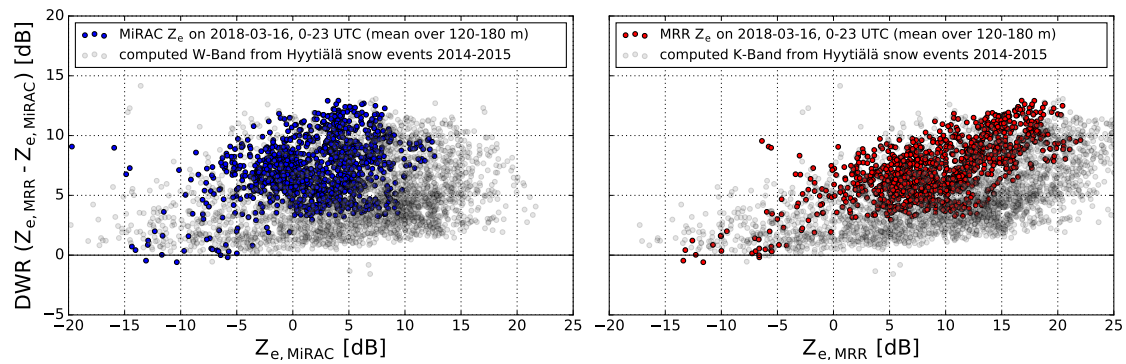
Figure A.10: Left: Dual Wavelength Ratio (DWR) of MRR (K-Band) minus MiRAC (W-Band) reflectivities against the MiRAC (W-Band) Z_e. In blue the measured values on February 3rd 2018 between 00:00 and 23:00 UTC at the site in Ny-Ålesund and in light grey computed values with a dataset from the measurement site in Hyytiälä of 5-minute snow measurements for two consecutive winters 2014/2015 and simulations of backscatter cross sections. Right: Similar to left, but DWR against MRR (K-Band) with the measured reflectivities in red.

List of Figures

References

AMAP, Snow, Water, Ice and Permafrost in the Arctic (SWIPA): Climate Change and the Cryosphere. - Chapter 4: Changing Snow Cover and its Impacts, Arctic Monitoring and Assessment Programme (AMAP), Oslo, Norway, 2011.

Battaglia, A., E. Rustemeier, A. Tokay, U. Blahak, and C. Simmer, PARSIVEL snow observations: A critical assessment, *Journal of Atmospheric and Oceanic Technology*, 27, 333–344, 2010.

Böhm, H. P., A General Equation for the Terminal Fall Speed of Solid Hydrometeors, *Journal of the Atmospheric Sciences*, 46, 2419–2427, 1989.

Bringi, V. N. and V. Chandrasekar, *Polarimetric Doppler Weather Radar: Principles and Applications*, Cambridge University Press, 2001.

Førland, E. J., R. Benestad, I. Hanssen-Bauer, J. E. Haugen, and T. E. Skaugen, Temperature and Precipitation Development at Svalbard 1900–2100, *Advances in Meteorology*, 2011, 1–14, 2012.

Fujiyoshi, Y., T. Endoh, T. Yamada, K. Tsuboki, Y. Tachibana, and G. Wakahama, Determination of a Z - R Relationship for Snowfall Using a Radar and High Sensitivity Snow Gauges, *Journal of Applied Meteorology*, 29, 147–152, 1990.

Gergely, M., S. J. Cooper, and T. J. Garrett, Using snowflake surface-area-to-volume ratio to model and interpret snowfall triple-frequency radar signatures, *Atmospheric Chemistry and Physics*, 17, 12011–12030, 2017.

Gunn, K. L. S. and J. S. Marshall, The distribution with size of aggregate snowflakes, *Journal of Meteorology*, 15, 452–461, 1958.

Hari, P. and M. Kulmala, Station for measuring ecosystem-atmosphere relations: SMEAR, *Boreal Environment Research*, 9789400756, 315–322, 2005.

Hersbach, H. and L. Dick, ERA5 reanalysis is in production, *ECMWF Newsletter*, 147, 7, 2016.

Heymsfield, A. J., S. Y. Matrosov, and N. B. Wood, Toward improving ice water content and snow-rate retrievals from radars. Part I: X and W bands, emphasizing cloudsat, *Journal of Applied Meteorology and Climatology*, 55, 2063–2090, 2016.

Huang, G.-J. J., V. N. Bringi, R. Cifelli, D. Hudak, and W. A. Petersen, A methodology to derive radar reflectivity-liquid equivalent snow rate relations using C-band

radar and a 2D video disdrometer, *Journal of Atmospheric and Oceanic Technology*, 27, 637–651, 2010.

Imai, I., M. Fujiwara, I. Ichimura, and Y. Toyama, Radar Reflectivity, *Papers of Meteorolgoy Geophysics*, 6, 130–139, 1955.

IPCC, Contribution of working group i to the fourth assessment report of the intergovernmental panel on climate change, in *Climate Change 2007: The Physical Science Basis*, edited by S. Solomon, D. Qin, M. Manning, Z. Chen, M. Marquis, K. B. Averyt, M. Tignor, and H. L. Miller, Cambridge Univ. Press, New York, 2007.

Kahnert, F. M., Numerical methods in electromagnetic scattering theory, *Journal of Quantitative Spectroscopy and Radiative Transfer*, 79-80, 775–824, 2003.

Kneifel, S., *Characterization of snowfall using ground − based passive and active remote sensors*, Doctoral thesis, Universität zu Köln, 2011.

Kneifel, S., M. S. Kulie, and R. Bennartz, A triple-frequency approach to retrieve microphysical snowfall parameters, *Journal of Geophysical Research*, 116, D11203, 2011a.

Kneifel, S., M. Maahn, G. Peters, and C. Simmer, Observation of snowfall with a low-power FM-CW K-band radar (Micro Rain Radar), *Meteorology and Atmospheric Physics*, 113, 75–87, 2011b.

Kneifel, S., A. Von Lerber, J. Tiira, D. Moisseev, P. Kollias, and J. Leinonen, Observed relations between snowfallmicrophysics and triple-frequency radar measurements, *Journal of Geophysical Research: Atmospheres*, 120, 6034–6055, 2015.

Kochendorfer, J., R. Nitu, M. Wolff, E. Mekis, R. Rasmussen, B. Baker, M. E. Earle, A. Reverdin, K. Wong, C. D. Smith, D. Yang, Y. A. Roulet, S. Buisan, T. Laine, G. Lee, J. L. C. Aceituno, J. Alastrué, K. Isaksen, T. Meyers, R. Brækkan, S. Landolt, A. Jachcik, and A. Poikonen, Analysis of single-Alter-shielded and unshielded measurements of mixed and solid precipitation from WMO-SPICE, *Hydrology and Earth System Sciences*, 21, 3525–3542, 2017.

Kollias, P., B. A. Albrecht, and F. D. Marks Jr., Why Mie?, *Bulletin of the American Meteorological Society*, 2002.

Kollias, P., E. E. Clothiaux, M. A. Miller, B. A. Albrecht, G. L. Stephens, and T. P. Ackerman, Millimeter-Wavelength Radars : New Frontier in Atmospheric Cloud

and Precipitation Research, *Bulletin of the American Meteorological Society*, 88, 1608–1624, 2007.

Kruger, A. and W. F. Krajewski, Two-dimensional video disdrometer: A description, *Journal of Atmospheric and Oceanic Technology*, 19, 602–617, 2002.

Küchler, N., S. Kneifel, U. Löhnert, P. Kollias, H. Czekala, and T. Rose, A W-band radar-radiometer system for accurate and continuous monitoring of clouds and precipitation, *Journal of Atmospheric and Oceanic Technology*, 34, 2375–2392, 2017.

Kulie, M. S. and R. Bennartz, Utilizing spaceborne radars to retrieve dry snowfall, *Journal of Applied Meteorology and Climatology*, 48, 2564–2580, 2009.

Langille, R. C. and R. S. Thain, Some quantitative measurements of 3 cm radar echos from falling snow, *Canadian Journal of Physics*, 29, 482–490, 1951.

Leinonen, J., Python code for T-matrix scattering calculations, available at: `https://github.com/jleinonen/pytmatrix/`, 2018, Accessed: 08/24/2018.

Leinonen, J., S. Kneifel, D. Moisseev, J. Tyynelä, S. Tanelli, and T. Nousiainen, Evidence of nonspheroidal behavior in millimeter-wavelength radar observations of snowfall, *Journal of Geophysical Research Atmospheres*, 117, 1–10, 2012.

Leinonen, J. and D. Moisseev, What do triple-frequency radar signatures reveal about aggregate snowflakes?, *Journal of Geophysical Research*, 120, 229–239, 2015.

Leinonen, J. and W. Szyrmer, Radar signatures of snowflake riming: A modeling study, *Earth and Space Science*, 2, 346–358, 2015.

Levizzani, V., S. Laviola, and E. Cattani, Detection and measurement of snowfall from space, *Remote Sensing*, 3, 145–166, 2011.

Lhermitte, R., A 94-GHz Doppler Radar for Cloud Observations, *Journal of Atmospheric and Oceanic Technology*, 4, 36–48, 1987.

Lhermitte, R., Observation of rain at vertical incidence with a 94 GHz Doppler radar: An insight on Mie scattering, *Geophysical Research Letters*, 15, 1125–1128, 1988.

Libbrecht, K. G., The physics of snow crystals, *Reports on Progress in Physics*, 68, 855–895, 2005.

Lindsay, R., M. Wensnahan, A. Schweiger, and J. Zhang, Evaluation of seven differ-
ent atmospheric reanalysis products in the arctic, *Journal of Climate*, 27, 2588–
2606, 2014.

Liu, G., Deriving snow cloud characteristics from CloudSat observations, *Journal of
Geophysical Research Atmospheres*, 114, 1–13, 2008.

Locatelli, J. D. and P. V. Hobbs, Fall speeds and masses of solid precipitation
particles, *Journal of Geophysical Research*, 79, 2185–2197, 1974.

Lohmann, U., F. Lüönd, and F. Mahrt, *An Introduction to Clouds. From the Mi-
croscale to Climate*, Cambridge University Press, 2016.

López-Moreno, J. I., J. Boike, A. Sanchez-Lorenzo, and J. W. Pomeroy, Impact
of climate warming on snow processes in Ny-Alesund, a polar maritime site at
Svalbard, *Global and Planetary Change*, 146, 10–21, 2016.

Maahn, M., C. Burgard, S. Crewell, I. V. Gorodetskaya, S. Kneifel, S. Lhermitte,
K. Van Tricht, and N. P. M. van Lipzig, How does the spaceborne radar blind zone
affect derived surface snowfall statistics in polar regions?, *Journal of Geophysical
Research*, 119, 13604–13620, 2014.

Maahn, M. and P. Kollias, Improved Micro Rain Radar snow measurements using
Doppler spectra post-processing, *Atmospheric Measurement Techniques*, 5, 2661–
2673, 2012.

Magono, C. and T. Nakamura, Aerodynamic Studies of Falling Snowflakes, *Journal
of the Meteorological Society of Japan*, 43, 139–147, 1965.

Marshall, J. S. and K. L. S. Gunn, Measurement of Snow Parameters by Radar,
Journal of Meteorology, 9, 322–327, 1952.

Marshall, J. S. and W. M. Palmer, The distribution of raindrops with size, *Journal
of Meteorology*, 5(4), 165–166, 1948.

Matrosov, S. Y., C. Campbell, D. Kingsmill, and E. Sukovich, Assessing snowfall
rates from X-Band radar reflectivity measurements, *Journal of Atmospheric and
Oceanic Technology*, 26, 2324–2339, 2009.

Matrosov, S. Y., M. D. Shupe, and I. V. Djalalova, Snowfall retrievals using
millimeter-wavelength cloud radars, *Journal of Applied Meteorology and Clima-
tology*, 47, 769–777, 2008.

Maturilli, M., A. Herber, and G. König-Langlo, Climatology and time series of surface meteorology in Ny-Ålesund, Svalbard, *Earth System Science Data*, 5, 155–163, 2013.

Mech, M., L.-l. Kliesch, A. Anhäuser, T. Rose, P. Kollias, and S. Crewell, Microwave Radar / radiometer for Arctic Clouds MiRAC : First insights from the ACLOUD campaign, *Atmospheric Measurement Techniques Discussions*, pages 1–32, in review, 2019.

Merkouriadi, I., J.-C. Gallet, R. M. Graham, G. E. Liston, C. Polashenski, A. Rösel, and S. Gerland, Winter snow conditions on Arctic sea ice north of Svalbard during the Norwegian young sea ICE (N-ICE2015) expedition, *Journal of Geophysical Research: Atmospheres*, 112, 10,837–10,854, 2017.

Mishchenko, M. I., Particle in a Fixed Orientation, *Applied Optics*, 39, 1026–1031, 2000.

Moisseev, D., Snow microphysical properties retrieved from PIP observations collected in Hyytiala on 2014-2015, available at `https://github.com/dmoisseev/Snow-Retrievals-2014-2015`, 2018, Accessed: 08/24/2018.

Moisseev, D., A. von Lerber, and J. Tiira, Quantifying the effect of riming on snowfall using ground-based observations, *Journal of Geophysical Research*, 122, 4019–4037, 2017.

Moisseev, D. N. and V. Chandrasekar, Examination of the μ–Λ relation suggested for drop size distribution parameters, *Journal of Atmospheric and Oceanic Technology*, 24, 847–855, 2007.

Neuber, R., A multi-disciplinary Arctic research facility: From the Koldewey - Rabot - Corbel - Stations to the AWI-IPEV research base on Spitsbergen, *Polarforschung*, 73, 117–123, 2006.

Newman, A. J., P. A. Kucera, and L. F. Bliven, Presenting the Snowflake Video Imager (SVI), *Journal of Atmospheric and Oceanic Technology*, 26, 167–179, 2009.

Nitu, R., Y. Roulet, M. Wolff, M. Earle, A. Reverdin, C. Smith, J. Kochendorfer, S. Morin, R. Rasmussen, K. Wong, J. Alastrué, L. Arnold, B. Baker, S. Buisan, J. L. Collado, M. Colli, B. Collins, A. Gaydos, H.-R. Hannula, J. Hoover, P. Joe, A. Kontu, T. Laine, L. Lanza, E. Lanzinger, G. W. Lee, Y. Lejeune, L. Leppänen, E. Mekis, J. Panel, A. Poikonen, S. Ryu, F. Sabatini, J. Theriault, D. Yang, C. Genthon, F. van den Heuvel, N. Hirasawa, H. Konishi, K. Nishimura, and

A. Senese, WMO Solid Precipitation Intercomparison Experiment (SPICE) (2012-2015), Technical Report Instruments and Observing Methods Report No. 131, World Meteorological Organization, 2018.

Nomokonova, T., K. Ebell, U. Löhnert, M. Maturilli, C. Ritter, and E. O'Connor, Statistics on clouds and their relation to thermodynamic conditions at Ny-Ålesund using ground-based sensor synergy, *Atmospheric Chemistry and Physics Discussions*, pages 1–37, 2019.

OTT, *Operating Instructions Precipitation gauge OTT Pluvio² L*, 2016a.

OTT, *Operating instructions Present Weather Sensor Parsivel*, 2016b.

Petty, G. W., *A First Course in Atmospheric Radiation*, Sundog Publishing, second edition, 2006.

Pruppacher, H. R. and J. D. Klett, *Microphysics of Clouds and Precipitaiton*, volume 2, Kluwer Academic Publishers, 1997.

Rasmussen, R., B. Baker, J. Kochendorfer, T. Meyers, S. Landolt, A. P. Fischer, J. Black, J. M. Thériault, P. Kucera, D. Gochis, C. Smith, R. Nitu, M. Hall, K. Ikeda, and E. Gutmann, How well are we measuring snow: The NOAA/-FAA/NCAR winter precipitation test bed, *Bulletin of the American Meteorological Society*, 93, 811–829, 2012.

Rasmussen, R., M. Dixon, S. Vasiloff, F. Hage, S. Knight, J. Vivekanandan, and M. Xu, Snow Nowcasting Using a Real-Time Correlation of Radar Reflectivity with Snow Gauge Accumulation, *Journal of Applied Meteorology*, 42, 20–36, 2003.

Rose, T., S. Crewell, U. Löhnert, and C. Simmer, A network suitable microwave radiometer for operational monitoring of the cloudy atmosphere, *Atmospheric Research*, 75, 183–200, 2005.

Serreze, M. C. and R. G. Barry, Processes and impacts of Arctic amplification: A research synthesis, *Global and Planetary Change*, 77, 85–96, 2011.

Souverijns, N., A. Gossart, S. Lhermitte, I. V. Gorodetskaya, S. Kneifel, M. Maahn, F. L. Bliven, and N. P. M. M. van Lipzig, Estimating radar reflectivity - Snowfall rate relationships and their uncertainties over Antarctica by combining disdrometer and radar observations, *Atmospheric Research*, 196, 211–223, 2017.

Stephens, G. L., D. G. Vane, R. J. Boain, G. G. Mace, K. Sassen, Z. Wang, A. J. Illingworth, E. J. O'Connor, W. B. Rossow, S. L. Durden, S. D. Miller, R. T.

Austin, A. Benedetti, C. Mitrescu, and the CloudSat Science Team, The CloudSat mission and the A-Train, *Bulletin of the American Meteorological Society*, 83, 1771–1790, 2002.

Szyrmer, W. and I. Zawadzki, Snow Studies. Part II: Average Relationship between Mass of Snowflakes and Their Terminal Fall Velocity, *Journal of the Atmospheric Sciences*, 67, 3319–3335, 2010.

Tecla Falconi, M., A. Von Lerber, D. Ori, F. Silvio Marzano, and D. Moisseev, Snowfall retrieval at X, Ka and W bands: Consistency of backscattering and microphysical properties using BAECC ground-based measurements, *Atmospheric Measurement Techniques*, 11, 3059–3079, 2018.

Tiira, J., D. N. Moisseev, A. von Lerber, D. Ori, A. Tokay, L. F. Bliven, and W. Petersen, Ensemble mean density and its connection to other microphysical properties of falling snow as observed in Southern Finland, *Atmospheric Measurement Techniques*, 9, 4825–4841, 2016.

Tyynelä, J., J. Leinonen, D. Moisseev, and T. Nousiainen, Radar backscattering from snowflakes: Comparison of fractal, aggregate, and soft spheroid models, *Journal of Atmospheric and Oceanic Technology*, 28, 1365–1372, 2011.

von Lerber, A., *Challenges in measuring winter precipitation:*, Doctoral thesis, Aalto University, 2018.

von Lerber, A., D. Moisseev, L. F. Bliven, W. Petersen, A.-M. M. Harri, and V. Chandrasekar, Microphysical properties of snow and their link to Ze–S relations during BAECC 2014, *Journal of Applied Meteorology and Climatology*, 56, 1561–1582, 2017.

von Lerber, A., D. Moisseev, D. A. Marks, W. Petersen, A. M. Harri, and V. Chandrasekar, Validation of GMI snowfall observations by using a combination of weather radar and surface measurements, *Journal of Applied Meteorology and Climatology*, 57, 797–820, 2018.

Wolff, M. A., K. Isaksen, A. Petersen-ØVerleir, K. Ødemark, T. Reitan, and R. Brækkan, Derivation of a new continuous adjustment function for correcting wind-induced loss of solid precipitation: Results of a Norwegian field study, *Hydrology and Earth System Sciences*, 19, 951–967, 2015.

B   Acknowledgments